An explicit pseudo-energy conserving time-integration scheme for Hamiltonian dynamics

Frédéric Marazzato, Alexandre Ern, Christian Mariotti, Laurent Monasse

An explicit pseudo-energy conserving time-integration scheme for Hamiltonian dynamics

Frédéric Marazzato[1,2,3], Alexandre Ern[1,3], Christian Mariotti[2] and Laurent Monasse[1,4]

[1]Université Paris-Est, Cermics (ENPC), F-77455 Marne-la-Vallée cedex 2, France
email: {alexandre.ern, frederic.marazzato}@enpc.fr

[2]CEA, DAM, DIF, F-91297 Arpajon, France
email: christian.mariotti@cea.fr

[3]Inria Paris, EPC SERENA, F-75589 Paris, France

[4] Inria, Team COFFEE, Sophia Antipolis and Université Nice Sophia Antipolis, CNRS and Laboratoire J. A. Dieudonné, UMR 7351, 06108 Nice, France
email: laurent.monasse@inria.fr

December 29, 2018

Abstract

We propose a new explicit pseudo-energy and momentum conserving scheme for the time integration of Hamiltonian systems. The scheme, which is formally second-order accurate, is based on two key ideas: the integration during the time-steps of forces between free-flight particles and the use of momentum jumps at the discrete time nodes leading to a two-step formulation for the acceleration. The pseudo-energy conservation is established under exact force integration, whereas it is valid to second-order accuracy in the presence of quadrature errors. Moreover, we devise an asynchronous version of the scheme that can be used in the framework of slow-fast time-stepping strategies. The scheme is validated against classical benchmarks and on nonlinear or inhomogeneous wave propagation problems.

1 Introduction

Energy and momentum conservation is an important property of numerical schemes for a large number of physical problems. For instance, in statistical physics, accurately conserving first integrals constitutes a fundamental requirement to capture the correct behaviour of the system. In mechanics, conservation of the mechanical energy (together with momentum) is an important feature for systems such as the acoustics in a piano [3] or nonlinear contact dynamics [12, 5]. In this work, we consider Hamiltonian systems consisting of N particles in dimension d (typically, $d = 1$, 2 or 3) where $q_i, p_i \in \mathbb{R}^d$ are the position and momentum of the particle $i \in \{1, \dots, N\}$. We assume that the Hamiltonian has the following split form:

$$H(\boldsymbol{q}, \boldsymbol{p}) = \frac{1}{2}\boldsymbol{p}^{\mathrm{T}}\boldsymbol{M}^{-1}\boldsymbol{p} + V(\boldsymbol{q}), \tag{1}$$

where $\boldsymbol{q} = (q_1, \dots, q_N) \in \mathbb{R}^{dN}$ is the position vector of the particles, $\boldsymbol{p} = (p_1, \dots, p_N) \in \mathbb{R}^{dN}$ is the momentum vector of the particles, $\boldsymbol{M}$ is the symmetric positive definite mass

matrix and V is the potential energy. The system is thus driven by the equations

$$\dot{\boldsymbol{q}} = \boldsymbol{M}^{-1}\boldsymbol{p}, \qquad \dot{\boldsymbol{p}} = -\nabla V(\boldsymbol{q}). \tag{2}$$

Several approaches have been proposed to tackle the issue of conservation when integrating numerically (2). A first possibility consists in the use of symplectic schemes [11], which integrate a modified (not explicitly exhibited, except in certain simple cases) Hamiltonian and thus preserve the first integrals of the dynamics over exponentially long times (with respect to the time-step), up to fluctuations whose amplitudes grow with the time-step. However, in the case of variable time-steps, symplectic schemes lose their conservation properties since the modified Hamiltonian changes with the time-step [1]. When the time-step size is driven by the shape of the Hamiltonian (e.g. in Kepler's problem with high eccentricity), a workaround consists in adding a perturbation accounting for the time-step variation in order for a rescaled dynamic to remain Hamiltonian [9]. In practice, for mechanical problems, such a condition on the time-step can become impractical, since the time-step could be imposed due to coupling or stiffness phenomena not accounted for in the Hamiltonian part. For an extended review of variational integrators in mechanics, we refer the reader to [21]. Another approach consists in imposing the exact conservation of energy and momentum at each step of the numerical scheme. Integrating on the constant energy manifold can be carried out using projection [13] or Lie group integration [14], but these methods are computationally expensive as soon as the manifold of constant energy and momentum has a complex shape. Another class of methods, energy-momentum conserving schemes, have been proposed in [24, 7, 12, 3] for nonlinear mechanics, contact mechanics and nonlinear wave equations, among others. The general principle is to integrate the nonlinear forces at a special time during the time-step, which is determined through a nonlinear implicit procedure. A higher-order version of these implicit schemes has been derived for linear wave propagation in [2]. Variational integrators combining features of symplectic and energy-momentum schemes have been developed for variable time-step strategies [15] and nonlinear mechanical problems in [8].

To the best of our knowledge, no explicit pseudo-energy conserving scheme has been proposed to date for nonlinear problems. With the motivation that explicit schemes often result in greater computational efficiency, the goal of the present work is to develop such an explicit scheme for nonlinear mechanics, where pseudo-energy conservation holds exactly for exact force integration and up to second-order accuracy in the presence of quadratures. The present scheme hinges on two key ideas. The first one, already considered in [20], is to approximate the dynamics of the particles by free-flight trajectories during each time-step. The second one is to use momentum jumps at the discrete time nodes to approximate the acceleration. In doing so, we circumvent the negative result on the existence of explicit schemes in [3, Lemma 3.3] through the use of a two-step strategy. This idea has some links with the implicit energy-conserving average vector field method [22] where the conservation of the Hamiltonian is formulated using an implicit integral of the forces derived from the potential V over the time-step. A high-order generalization of the average vector field method using collocation has been developed in [10]. The present numerical scheme shares with average vector field methods the salient feature of average force integration over each time-step. However, the two schemes differ on the discretisation of the acceleration, which is based here on momentum jumps.

A further development of the present work is to devise an asynchronous version of our scheme that lends itself to slow-fast decompositions as presented in [11], with the goal to further reduce the computational cost of the simulation. In the case of mechanical systems with local stiffness, the conditional stability of an explicit time-integration

scheme typically involves small time-steps for the whole system. A promising direction to mitigate this drawback consists in using a local time-stepping strategy. In the linear case, explicit high-order energy-momentum conserving methods with local time-stepping have been proposed in [4]. In the nonlinear case, a modified Störmer–Verlet method for Hamiltonian systems containing slow and fast components is developed in [11]. It is proved that this time-integrator remains symplectic, but the ratio of the fast and slow time-steps strongly influences the error on the total energy and, in general, a good balance has to be found experimentally. This phenomenon is called resonance since it is encountered for certain slow/fast ratios. Similarly, asynchronous variational integrators generally exhibit resonances when the local time-steps are close to certain rational ratios, so that ensuring stability requires adequate fitting of the local time-steps [6]. In contrast, the asynchronous version of the present scheme allows one to make slow-fast time-integration while conserving a pseudo-energy (in the absence of quadrature errors). Our numerical tests show that the asynchronous scheme still exhibits second-order accuracy; a mathematical proof of this property is postponed to future work.

This paper is organized as follows. In Section 2, we present the scheme for a Hamiltonian system of interacting particles with a synchronous time-integration and establish the main properties of the scheme including second-order accuracy, time-reversibility, linear stability under a CFL condition, and pseudo-energy conservation under exact force integration. In Section 3 we test the synchronous scheme on various benchmarks from the literature including a nonlinear wave propagation problem. In Section 4, we present the slow-fast time-stepping capabilities of the asynchronous version of the scheme, together with numerical results on model particle systems connected by springs and on an inhomogeneous wave equation. These results demonstrate the efficiency gains of the asynchronous scheme with respect to the synchronous scheme.

2 Synchronous scheme

In this section, we present our scheme in its synchronous version and establish its main properties.

2.1 Definition of the scheme

We consider a sequence of discrete time nodes t^n, $n = 0, 1, \ldots$, with time-steps $h_n = t^{n+1} - t^n$ and time intervals $I_n = [t^n, t^{n+1}]$. The scheme is written at step n as follows: knowing $\boldsymbol{p}^{n-1/2}$, $\boldsymbol{q}^n$, and $[\boldsymbol{p}]^n$, one computes

$$\boldsymbol{p}^{n+1/2} = \boldsymbol{p}^{n-1/2} + [\boldsymbol{p}]^n, \tag{3a}$$

$$\boldsymbol{q}^{n+1} = \boldsymbol{q}^n + h_n \boldsymbol{M}^{-1} \boldsymbol{p}^{n+1/2}, \tag{3b}$$

$$\frac{1}{2}\left([\boldsymbol{p}]^{n+1} + [\boldsymbol{p}]^n\right) = -\int_{I_n} \nabla V(\hat{\boldsymbol{q}}^n(t))dt, \tag{3c}$$

with the free-flight trajectory over the time interval I_n defined by

$$\hat{\boldsymbol{q}}^n(t) = \boldsymbol{q}^n + (t - t^n)\boldsymbol{M}^{-1}\boldsymbol{p}^{n+1/2} \quad \forall t \in I_n. \tag{4}$$

Here, $[\boldsymbol{p}]^n$ represents the jump of the momentum vector at time t^n, $\boldsymbol{q}^n$ the position vector at time t^n, and $\boldsymbol{p}^{n+1/2}$ is the momentum vector between t^n and t^{n+1}. We observe that $\boldsymbol{q}^{n+1} = \hat{\boldsymbol{q}}^n(t^{n+1})$. We initialize the scheme as follows:

$$\boldsymbol{p}^{-1/2} = \boldsymbol{p}(t^0), \quad \boldsymbol{q}^0 = \boldsymbol{q}(t^0), \quad [\boldsymbol{p}]^0 = \boldsymbol{0}, \tag{5}$$

where $\boldsymbol{q}(t^0), \boldsymbol{p}(t^0)$ are the given position and momentum vectors at the initial time t^0. The scheme (3) can alternatively be written as the following 2-step scheme without jumps: knowing $\boldsymbol{p}^{n-1/2}$, $\boldsymbol{q}^n$, and $\boldsymbol{p}^{n+1/2}$, one computes

$$\boldsymbol{q}^{n+1} = \boldsymbol{q}^n + h_n \boldsymbol{M}^{-1} \boldsymbol{p}^{n+1/2}, \tag{6a}$$

$$\frac{1}{2}\left(\boldsymbol{p}^{n+3/2} - \boldsymbol{p}^{n-1/2}\right) = -\int_{I_n} \nabla V(\hat{\boldsymbol{q}}^n(t))dt, \tag{6b}$$

with the free-flight trajectory defined by (4). The initialization of the scheme, equivalent to (5), is as follows:

$$\boldsymbol{p}^{-1/2} = \boldsymbol{p}(t^0), \quad \boldsymbol{q}^0 = \boldsymbol{q}(t^0), \quad \boldsymbol{p}^{1/2} = \boldsymbol{p}(t^0). \tag{7}$$

This initialization is tailored to achieve exact pseudo-energy conservation under exact force integration, as shown in Theorem 1 below. Other choices for the initialization are possible, for instance using a one-step method.

In the numerical implementation of the scheme, the integral in (3c) (or in (6b)) is usually not computed exactly but with a quadrature of the form

$$Q_n(f(t); t^n; t^{n+1}) = h_n \sum_{i=0}^{I} \omega_i f(\lambda_i t^n + (1-\lambda_i) t^{n+1}) \approx \int_{I_n} f(t)dt, \tag{8}$$

where the real numbers ω_i are the weights and the real numbers $\lambda_i \in [0,1]$ define the quadrature points. Applying the quadrature componentwise for the calculation of the forces and exploiting that the position of the particles varies linearly in time during the free flight, we obtain

$$Q_n\left(\nabla V(\hat{\boldsymbol{q}}^n(t)); t^n; t^{n+1}\right) = h_n \sum_{i=0}^{I} \omega_i \nabla V(\lambda_i \boldsymbol{q}^n + (1-\lambda_i)\boldsymbol{q}^{n+1})) \approx \int_{I_n} \nabla V(\hat{\boldsymbol{q}}^n(t))dt, \tag{9}$$

and we replace (3c) with

$$\frac{1}{2}\left([\boldsymbol{p}]^{n+1} + [\boldsymbol{p}]^n\right) = -Q_n\left(\nabla V(\hat{\boldsymbol{q}}^n(t)); t^n; t^{n+1}\right), \tag{10}$$

and a similar modification for (6b). In what follows, we assume that the quadrature is symmetric:

$$\forall i \in \{0, \dots, I\}, \quad \omega_i = \omega_{I-i} \quad \text{and} \quad \lambda_i = 1 - \lambda_{I-i}, \tag{11}$$

and at least of order two (i.e., that the quadrature integrates exactly affine polynomials). We also assume that V is of class C^2, i.e., $V \in C^2(\mathbb{R}^{dN}; \mathbb{R})$. This implies that

$$Q_n\left(\nabla V(\hat{\boldsymbol{q}}^n(t)); t^n; t^{n+1}\right) = \int_{I_n} \nabla V(\hat{\boldsymbol{q}}^n(t))dt + \mathcal{O}(h_n^3). \tag{12}$$

2.2 Properties of the scheme

We now establish various properties of the scheme: pseudo-energy conservation (in the absence of quadrature errors), symmetry (or time-reversibility), second-order accuracy, and linear stability (with constant time-step).

Theorem 1 (Pseudo-energy conservation)**.** *Assume that the quadrature is exact. Then, the scheme (3) exactly conserves the following pseudo-energy:*

$$\tilde{H}^n = V(\boldsymbol{q}^n) + \frac{1}{2}\left(\boldsymbol{p}^{n-1/2}\right)^{\mathrm{T}} \boldsymbol{M}^{-1} \boldsymbol{p}^{n+1/2}. \tag{13}$$

Moreover, denoting $H^0 := H(\boldsymbol{q}(t^0), \boldsymbol{p}(t^0))$ the value of the exact Hamiltonian at the initial time time t^0, we have $\tilde{H}^n = H^0$ for all $n \geq 0$ if the scheme is initialized using (5).

Proof. Using (3.a), (4), and the chain rule, we obtain

$$\frac{d}{dt}\left(V(\hat{\boldsymbol{q}}^n(t))\right) = \nabla V\left(\hat{\boldsymbol{q}}^n(t)\right)\cdot(\hat{\boldsymbol{q}}^n)'(t) = \left(\boldsymbol{M}^{-1}\boldsymbol{p}^{n+1/2}\right)^{\mathrm{T}}\nabla V\left(\hat{\boldsymbol{q}}^n(t)\right).$$

Integrating in time and using (3c) and the symmetry of $\boldsymbol{M}$, we infer that

$$\begin{aligned} V(\boldsymbol{q}^{n+1}) - V(\boldsymbol{q}^n) &= \left(\boldsymbol{p}^{n+1/2}\right)^{\mathrm{T}}\boldsymbol{M}^{-1}\int_{t^n}^{t^{n+1}}\nabla V(\hat{\boldsymbol{q}}^n(t))dt \\ &= -\left(\boldsymbol{p}^{n+1/2}\right)^{\mathrm{T}}\boldsymbol{M}^{-1}\frac{1}{2}\left([\boldsymbol{p}]^{n+1} + [\boldsymbol{p}]^n\right) \\ &= -\left(\boldsymbol{p}^{n+1/2}\right)^{\mathrm{T}}\boldsymbol{M}^{-1}\frac{1}{2}\left(\boldsymbol{p}^{n+3/2} - \boldsymbol{p}^{n-1/2}\right). \end{aligned}$$

This leads to

$$V(\boldsymbol{q}^{n+1}) + \frac{1}{2}\left(\boldsymbol{p}^{n+1/2}\right)^{\mathrm{T}}\boldsymbol{M}^{-1}\boldsymbol{p}^{n+3/2} = V(\boldsymbol{q}^n) + \frac{1}{2}\left(\boldsymbol{p}^{n-1/2}\right)^{\mathrm{T}}\boldsymbol{M}^{-1}\boldsymbol{p}^{n+1/2},$$

showing that $\tilde{H}^{n+1} = \tilde{H}^n$, thereby proving the first assertion. Finally, using the initialization (5), we obtain $\tilde{H}^0 = H^0$, and this concludes the proof. □

Remark 2 (Quadratures)**.** *In practice, the integral in Equation (3c) can be computed exactly only for polynomial potentials V. For instance, using the n-point Gauss–Lobatto (resp., Gauss–Legendre) quadrature, polynomials of degree up to $2n-3$ (resp., $2n-1$) are integrated exactly. The use of quadratures instead of exact integration for general nonlinear potentials entails only an approximate conservation of the pseudo-energy. Since the scheme is second-order accurate (see Theorem 5 below), we expect that pseudo-energy conservation is second-order accurate at best:*

$$\tilde{H}^n = \tilde{H}^0 + O(h^2). \tag{14}$$

where $h = \sup_n h_n$. The order of the quadrature has an influence on the multiplicative constant in $O(h^2)$, with the constant (swiftly) decreasing when increasing the quadrature order. Numerical results are presented on a nonlinear wave propagation problem in Section 3.3.

Remark 3 (Momentum conservation)**.** *Let $(1,...,1)$ be the vector of size dN filled with ones. Assume that the system is isolated, i.e., $(1,..,1)^{\mathrm{T}}\cdot\nabla V(\boldsymbol{q}) = \boldsymbol{0}$ for all $\boldsymbol{q}\in\mathbb{R}^{dN}$. Then, the total momentum, defined as $P_{n+1/2} := (1,..,1)^{\mathrm{T}}\cdot\boldsymbol{p}_{n+1/2}$ for all $n\geq 0$, is conserved. This follows by taking the product of $(1,...,1)^{\mathrm{T}}$ with Equation (6b) and the null momentum jump initialisation condition in Equation (5).*

Proposition 4 (Symmetry)**.** *If the quadrature (9) is exact or symmetric, then the scheme (6) is symmetric (or time-reversible).*

Proof. Let $\boldsymbol{Y}^n = (\boldsymbol{q}^n, \frac{\boldsymbol{p}^{n-1/2}+\boldsymbol{p}^{n+1/2}}{2}, \boldsymbol{p}^{n+1/2} - \boldsymbol{p}^{n-1/2})^{\mathrm{T}}$. Since we are going to consider positive and negative time-steps in this proof, we denote by $\mathrm{sign}(h_n)$ the sign of the time-step. The numerical scheme can be written as $\boldsymbol{Y}^{n+1} = \boldsymbol{\Phi}_{h_n}(\boldsymbol{Y}^n)$, where for a generic column vector $\boldsymbol{Y} = (\boldsymbol{Y}_1, \boldsymbol{Y}_2, \boldsymbol{Y}_3)^{\mathrm{T}}$, we have

$$\boldsymbol{\Phi}_{h_n}(\boldsymbol{Y}) = \begin{pmatrix} \boldsymbol{Y}_1 + h_n\boldsymbol{M}^{-1}\left(\boldsymbol{Y}_2 + \dfrac{\mathrm{sign}(h_n)}{2}\boldsymbol{Y}_3\right) \\ \boldsymbol{Y}_2 - Q_n\left(\nabla V\left(\boldsymbol{Y}_1 + t\boldsymbol{M}^{-1}\left(\boldsymbol{Y}_2 + \dfrac{\mathrm{sign}(h_n)}{2}\boldsymbol{Y}_3\right)\right); 0; h_n\right) \\ -\boldsymbol{Y}_3 - 2\,\mathrm{sign}(h_n)Q_n\left(\nabla V\left(\boldsymbol{Y}_1 + t\boldsymbol{M}^{-1}\left(\boldsymbol{Y}_2 + \dfrac{\mathrm{sign}(h_n)}{2}\boldsymbol{Y}_3\right)\right); 0; h_n\right) \end{pmatrix},$$

where we used the invariance by translation of the quadrature Q_n. Therefore, we have

$$\boldsymbol{\Phi}_{-h_n}(\boldsymbol{Y}) = \begin{pmatrix} \boldsymbol{Y}_1 - h_n \boldsymbol{M}^{-1}\left(\boldsymbol{Y}_2 - \dfrac{\operatorname{sign}(h_n)}{2}\boldsymbol{Y}_3\right) \\ \boldsymbol{Y}_2 - Q_n\left(\nabla V\left(\boldsymbol{Y}_1 + t\boldsymbol{M}^{-1}\left(\boldsymbol{Y}_2 - \dfrac{\operatorname{sign}(h_n)}{2}\boldsymbol{Y}_3\right)\right); 0; -h_n\right) \\ -\boldsymbol{Y}_3 + 2\operatorname{sign}(h_n) Q_n\left(\nabla V\left(\boldsymbol{Y}_1 + t\boldsymbol{M}^{-1}\left(\boldsymbol{Y}_2 - \dfrac{\operatorname{sign}(h_n)}{2}\boldsymbol{Y}_3\right)\right); 0; -h_n\right) \end{pmatrix}.$$

It remains to verify that $\boldsymbol{\Phi}_{h_n} \circ \boldsymbol{\Phi}_{-h_n}(\boldsymbol{Y}) = \boldsymbol{Y}$ using that the quadrature is symmetric or exact. To fix the ideas, we assume that $h_n > 0$. Let us write $\boldsymbol{Y}' = \boldsymbol{\Phi}_{-h_n}(\boldsymbol{Y})$ and $\boldsymbol{Y}'' = \boldsymbol{\Phi}_{h_n}(\boldsymbol{Y}')$. Since $\boldsymbol{Y}_1' = \boldsymbol{Y}_1 - h_n\boldsymbol{M}^{-1}(\boldsymbol{Y}_2 - \frac{1}{2}\boldsymbol{Y}_3)$ and $\boldsymbol{Y}_2' + \frac{1}{2}\boldsymbol{Y}_3' = \boldsymbol{Y}_2 - \frac{1}{2}\boldsymbol{Y}_3$, we infer that

$$\boldsymbol{Y}_1'' = \boldsymbol{Y}_1' + h_n\boldsymbol{M}^{-1}\left(\boldsymbol{Y}_2' + \frac{1}{2}\boldsymbol{Y}_3'\right) = \boldsymbol{Y}_1. \tag{15}$$

For the second component, we obtain

$$\begin{aligned} \boldsymbol{Y}_2'' &= \boldsymbol{Y}_2' - Q_n\left(\nabla V\left(\boldsymbol{Y}_1 + (t-h_n)\boldsymbol{M}^{-1}\left(\boldsymbol{Y}_2 - \frac{1}{2}\boldsymbol{Y}_3\right)\right); 0; h_n\right) \\ &= \boldsymbol{Y}_2' - Q_n\left(\nabla V\left(\boldsymbol{Y}_1 + t\boldsymbol{M}^{-1}\left(\boldsymbol{Y}_2 - \frac{1}{2}\boldsymbol{Y}_3\right)\right); -h_n; 0\right) \\ &= \boldsymbol{Y}_2' + Q_n\left(\nabla V\left(\boldsymbol{Y}_1 + t\boldsymbol{M}^{-1}\left(\boldsymbol{Y}_2 - \frac{1}{2}\boldsymbol{Y}_3\right)\right); 0; -h_n\right) = \boldsymbol{Y}_2, \end{aligned}$$

where we used (15) in the first line and invariance by translation and symmetry of the quadrature Q_n in the second and third lines respectively. The proof that $\boldsymbol{Y}_3'' = \boldsymbol{Y}_3$ follows along similar lines. □

Theorem 5 (Consistency error)**.** *Assume that $V \in C^2(\mathbb{R}^{dN};\mathbb{R})$. If the quadrature (9) is exact or at least of order two, the scheme* (3) *has second-order accuracy in time.*

Proof. Let $\boldsymbol{q}(t), \boldsymbol{p}(t)$ be the exact solution to (2). Let us consider the column vector $\boldsymbol{Y}(t^n) = (\boldsymbol{q}(t^n), \frac{\boldsymbol{p}(t^{n-1/2})+\boldsymbol{p}(t^{n+1/2})}{2}, \boldsymbol{p}(t^{n+1/2}) - \boldsymbol{p}(t^{n-1/2}))^{\mathrm{T}}$. The consistency error is defined as

$$\boldsymbol{\eta}^{n+1} := \frac{\boldsymbol{Y}(t^{n+1}) - \boldsymbol{\Phi}_{h_n}(\boldsymbol{Y}(t^n))}{h_n},$$

where $\boldsymbol{\Phi}_{h_n}$ is defined in the previous proof. Let us denote by $\boldsymbol{\eta}_1^{n+1}, \boldsymbol{\eta}_2^{n+1}, \boldsymbol{\eta}_3^{n+1}$ the three components of the consistency error. We have

$$\begin{aligned} h_n\boldsymbol{\eta}_1^{n+1} &= \boldsymbol{q}(t^{n+1}) - \boldsymbol{q}(t^n) - h_n\boldsymbol{M}^{-1}\boldsymbol{p}(t^{n+1/2}), \\ h_n\boldsymbol{\eta}_2^{n+1} &= \frac{\boldsymbol{p}(t^{n+3/2}) - \boldsymbol{p}(t^{n-1/2})}{2} + Q_n\left(\nabla V(\check{\boldsymbol{q}}^n(t)); t^n; t^{n+1}\right), \\ h_n\boldsymbol{\eta}_3^{n+1} &= 2h_n\boldsymbol{\eta}_2^{n+1}, \end{aligned}$$

where $\check{\boldsymbol{q}}^n(t) = \boldsymbol{q}(t^n) + \boldsymbol{M}^{-1}\boldsymbol{p}(t^{n+1/2})(t-t^n)$. Using a Taylor expansion and the equation $\dot{\boldsymbol{q}}(t) = \boldsymbol{M}^{-1}\boldsymbol{p}(t)$, we infer that

$$h_n\boldsymbol{\eta}_1^{n+1} = h_n\dot{\boldsymbol{q}}(t^{n+1/2}) - h_n\boldsymbol{M}^{-1}\boldsymbol{p}(t^{n+1/2}) + \mathcal{O}(h_n^3) = \mathcal{O}(h_n^3).$$

Moreover, since the quadrature is of second-order (at least) so that it can be replaced by the mid-point quadrature up to $\mathcal{O}(h_n^3)$, and using the equations $\dot{\boldsymbol{q}}(t) = \boldsymbol{M}^{-1}\boldsymbol{p}(t)$ and

$\dot{\boldsymbol{p}}(t) = -\nabla V(\boldsymbol{q})(t)$, we obtain

$$\begin{aligned} h_n \boldsymbol{\eta}_2^{n+1} &= h_n \dot{\boldsymbol{p}}(t^{n+1/2}) - h_n \nabla V(\check{\boldsymbol{q}}(t^{n+1/2})) + \mathcal{O}(h_n^3) \\ &= h_n \dot{\boldsymbol{p}}(t^{n+1/2}) - h_n \nabla V(\boldsymbol{q}(t^n) + \tfrac{1}{2} h_n \dot{\boldsymbol{q}}(t^{n+1/2})) + \mathcal{O}(h_n^3) \\ &= h_n \dot{\boldsymbol{p}}(t^{n+1/2}) - h_n \nabla V(\boldsymbol{q}(t^{n+1/2})) + \mathcal{O}(h_n^3) = \mathcal{O}(h_n^3). \end{aligned}$$

We conclude that $\boldsymbol{\eta}^{n+1} = \mathcal{O}(h_n^2)$, i.e., the scheme is second-order accurate. □

Proposition 6 (Linear stability)**.** *Assume that the potential V is quadratic with a positive definite Hessian $\boldsymbol{H} := D^2V$. Let λ be the largest eigenvalue of $\boldsymbol{H}$. Let $\mu > 0$ be the smallest eigenvalue of $\boldsymbol{M}$. Then the scheme* (3) *is conditionally stable for a constant time-step h under the following CFL condition:*

$$h < 2\sqrt{\frac{\mu}{\lambda}}. \tag{16}$$

Proof. Since the potential V is quadratic, the dynamical system (2) is linear. Let $\boldsymbol{Z}^n$ be the column vector such that $\boldsymbol{Z}^n = \left(\boldsymbol{q}^n, \boldsymbol{p}^{n-1/2}, \boldsymbol{p}^{n+1/2}\right)^{\mathrm{T}}$. Adding a linear functional to V does not change the nature of the Hamiltonian system. We thus consider $\nabla V(\boldsymbol{0}) = \boldsymbol{0}$ and $V(\boldsymbol{0}) = 0$. Since $\nabla V(\boldsymbol{q})$ is by assumption linear in $\boldsymbol{q}$, we have $\nabla V(\hat{\boldsymbol{q}}^n(t)) = \nabla V(\boldsymbol{q}^n) + (t - t^n)\boldsymbol{H}\boldsymbol{M}^{-1}\boldsymbol{p}^{n+1/2}$, so that

$$\int_{I_n} \nabla V(\hat{\boldsymbol{q}}^n(t))dt = h\boldsymbol{H}\boldsymbol{q}^n + \frac{1}{2}h^2\boldsymbol{H}\boldsymbol{M}^{-1}\boldsymbol{p}^{n+1/2}.$$

Therefore, the scheme (3) can be written as $\boldsymbol{Z}^{n+1} = \boldsymbol{A}\boldsymbol{Z}^n$ with

$$\boldsymbol{A} = \begin{pmatrix} \boldsymbol{I}_{dN} & \boldsymbol{0}_{dN} & h\boldsymbol{M}^{-1} \\ \boldsymbol{0}_{dN} & \boldsymbol{0}_{dN} & \boldsymbol{I}_{dN} \\ -2h\boldsymbol{H} & \boldsymbol{I}_{dN} & -h^2\boldsymbol{H}\boldsymbol{M}^{-1} \end{pmatrix}.$$

The matrix $\boldsymbol{M}$ being symmetric definite positive, its square root $\boldsymbol{M}^{1/2}$ is well-defined. We then observe that

$$\begin{aligned} \tilde{\boldsymbol{A}} &= \begin{pmatrix} \boldsymbol{M}^{1/2} & \boldsymbol{0}_{dN} & \boldsymbol{0}_{dN} \\ \boldsymbol{0}_{dN} & \boldsymbol{M}^{-1/2} & \boldsymbol{0}_{dN} \\ \boldsymbol{0}_{dN} & \boldsymbol{0}_{dN} & \boldsymbol{M}^{-1/2} \end{pmatrix} \boldsymbol{A} \begin{pmatrix} \boldsymbol{M}^{-1/2} & \boldsymbol{0}_{dN} & \boldsymbol{0}_{dN} \\ \boldsymbol{0}_{dN} & \boldsymbol{M}^{1/2} & \boldsymbol{0}_{dN} \\ \boldsymbol{0}_{dN} & \boldsymbol{0}_{dN} & \boldsymbol{M}^{1/2} \end{pmatrix} \\ &= \begin{pmatrix} \boldsymbol{I}_{dN} & \boldsymbol{0}_{dN} & h\boldsymbol{I}_{dN} \\ \boldsymbol{0}_{dN} & \boldsymbol{0}_{dN} & \boldsymbol{I}_{dN} \\ -2h\boldsymbol{S} & \boldsymbol{I}_{dN} & -h^2\boldsymbol{S} \end{pmatrix}, \end{aligned}$$

where we introduced the symmetric positive definite matrix $\boldsymbol{S} = \boldsymbol{M}^{-1/2}\boldsymbol{H}\boldsymbol{M}^{-1/2}$. Up to an adequate change of variable for each of the coordinates, it is possible to assume that $\boldsymbol{S}$ is diagonal. Denoting $(\sigma_i)_{1\leq i\leq dN}$ the eigenvalues of $\boldsymbol{S}$ and scaling the momenta in $\boldsymbol{Z}_n$ by the factors $(\sqrt{2\sigma_i})_{1\leq i\leq dN}$, $-\tilde{\boldsymbol{A}}$ is block diagonal in the following matrices of order 3, for all $i \in \{1, \ldots, dN\}$:

$$a_i = \begin{pmatrix} -1 & 0 & -h\sqrt{2\sigma_i} \\ 0 & 0 & -1 \\ h\sqrt{2\sigma_i} & -1 & h^2\sigma_i \end{pmatrix}.$$

The characteristic polynomial χ_{a_i} of a_i is $\chi_{a_i}(X) = (X-1)(X^2 - X(h^2\sigma_i - 2) + 1)$, which shows that 1 is an eigenvalue of a_i. Moreover, the polynomial $X^2 - X(h^2\sigma_i - 2) + 1$ is

positive as long as $h < \frac{2}{\sqrt{\sigma_i}}$, and the two complex conjugate eigenvalues, written b_i and $\bar{b}_i$, have a modulus equal to 1. Thus, a_i can be diagonalized for all $i \in \{1, \dots, dN\}$. The case $h = \frac{2}{\sqrt{\sigma_i}}$ is excluded as, in that case, a_i has the single eigenvalue 1 with multiplicity three and a single eigenvector which prevents diagonalising a_i. Let P_i the matrix such that $P_i^{-1} a_i P_i = \mathrm{Diag}(1, b_i, \bar{b}_i)$. Then, writing P^{-1} the block-diagonal matrix composed of the elementary matrices $(P_i^{-1})_{1 \le i \le dN}$ and D the block-diagonal matrix composed of the diagonal matrices of eigenvalues of $(a_i)_{1 \le i \le dN}$, we infer that, for all $n \in \mathbb{N}$:

$$\|\tilde{\boldsymbol{A}}^n\| \le \|P^{-1}\| \|P\| \|D\|^n \le \|P^{-1}\| \|P\|,$$

because the diagonal matrix D has diagonal entries of modulus 1, and thus $\|D\| = 1$. Hence, for all $n \in \mathbb{N}$, we obtain $|\boldsymbol{Z}^n| \le C |\boldsymbol{Z}^0|$, for a constant C independent of n. Since the eigenvalues σ_i of $\boldsymbol{S}$ are positive and smaller than $\frac{\lambda}{\mu}$, we conclude that linear stability holds true under the CFL condition (16).

□

Remark 7 (Comparison with Störmer–Verlet)**.** *A possible writing of the Störmer–Verlet method is the following:*

$$\begin{aligned} \boldsymbol{q}^{n+1} &= \boldsymbol{q}^n + h_n \boldsymbol{M}^{-1} \boldsymbol{p}^{n+1/2}, \\ \boldsymbol{p}^{n+3/2} &= \boldsymbol{p}^{n+1/2} - h_{n+1} \nabla V(\boldsymbol{q}^{n+1}). \end{aligned}$$

Both the present scheme and the Störmer–Verlet scheme are of leapfrog-type, have a similar CFL condition for linear stability, and are second-order accurate. The main difference is that, using a mid-point quadrature, the forces used to update the momenta at t^{n+1} are computed at $t^{n+1/2}$ with the present scheme, i.e., $\frac{1}{2}(\boldsymbol{p}^{n+3/2} - \boldsymbol{p}^{n-1/2}) = -h_n \nabla V(\hat{\boldsymbol{q}}(t^{n+1/2}))$, whereas the momentum update can be rewritten as

$$\frac{1}{2}(\boldsymbol{p}^{n+3/2} - \boldsymbol{p}^{n-1/2}) = -\frac{1}{2}\Big(h_{n+1} \nabla V(\boldsymbol{q}^{n+1}) + h_n \nabla V(\boldsymbol{q}^n)\Big),$$

in the Störmer–Verlet scheme. Moreover, the origin of energy conservation is different for the two schemes. The Störmer–Verlet scheme is energy-conserving only for constant time-steps due to its symplecticity. The present scheme enjoys an algebraic pseudo-energy preservation property for every time-step (constant or not) up to quadrature errors.

Remark 8 (Adaptive time-stepping for discrete energy control)**.** *The conservation of the pseudo-energy does not imply stability since $\left(\boldsymbol{p}^{n-1/2}\right)^{\mathrm{T}} \boldsymbol{M}^{-1} \boldsymbol{p}^{n+1/2}$ does not have a sign a priori. However, defining the discrete energy*

$$H^n := V(\boldsymbol{q}^n) + \frac{1}{8}\left(\boldsymbol{p}^{n-1/2} + \boldsymbol{p}^{n+1/2}\right)^{\mathrm{T}} \boldsymbol{M}^{-1} \left(\boldsymbol{p}^{n-1/2} + \boldsymbol{p}^{n+1/2}\right), \tag{17}$$

a straightforward calculation shows that

$$H^n = \tilde{H}^n + \frac{1}{8}([\boldsymbol{p}]^n)^{\mathrm{T}} M^{-1} [\boldsymbol{p}]^n = \tilde{H}^n + \frac{1}{8} |M^{-1/2} [\boldsymbol{p}]^n|^2. \tag{18}$$

This implies that

$$0 \le H^n - \tilde{H}^n \le \mathcal{O}(h_n^2),$$

where we used the identity (18) for the lower bound and we invoked Theorem 5 for the upper bound. One can use the identity (18) during the computations for an on-the-fly monitoring of possible departures of the conserved pseudo-energy $\tilde{H}^n$ from the discrete energy H^n. The idea is to check whether $\frac{1}{8}|M^{-1/2}[\boldsymbol{p}]^n|^2 \le \epsilon_{fly} \tilde{H}^n$ after every momenta computation and to halve the time-step if this bound is not met (note that the momentum jumps converge to zero with the time-step). The benefits of such an adaptive time-stepping strategy are illustrated in Section 3.3.

3 Numerical results

In this section, we present numerical results for the scheme (3). We consider classical benchmarks from the literature and a nonlinear wave equation from [3].

3.1 Convergence study

We perform a convergence study with a single particle in dimension $d = 1$. The reference solution is $q(t) = \sin(t)^4 + 1$, and the corresponding potential energy is

$$V(q(t)) = 8\left((q(t) - 1)^{3/2} - (q(t) - 1)^2\right).$$

We apply the scheme (3) to this Hamiltonian system over 10^3 seconds using the mid-point quadrature as well as the three- and five-point Gauss–Lobatto quadratures of order 3 and 7, respectively, for the integration of the forces. We report the ℓ_1-error with respect to the reference solution (the sum of the errors at the discrete time nodes divided by the number of time-steps) in Figure 1 as a function of the number of force evaluations. We observe that for the three quadratures, the convergence is of second order as expected. The quadrature order does not impact the convergence rate but has an influence on the computational efficiency. We note that in this case, the mid-point quadrature is more efficient than the three- and five-point Gauss–Lobatto quadratures of order 3 and 7.

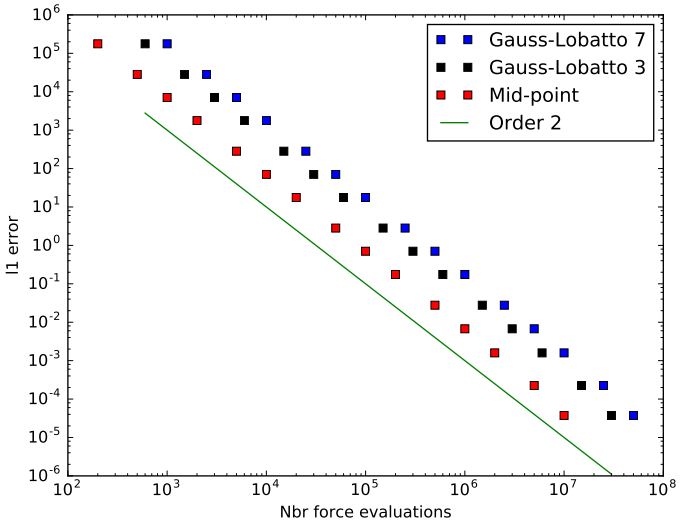

Figure 1: Convergence test: ℓ_1-convergence for a single particle

3.2 Fermi–Pasta–Ulam

This test case was proposed in [11, Chap. I.4]. It consists in having stiff linear springs linked to soft nonlinear springs in an alternating way, in dimension $d = 1$. Figure 2 illustrates the setting.

The Hamiltonian is

$$H(\boldsymbol{q}, \boldsymbol{p}) = \frac{1}{2}\sum_{i=1}^{m}(p_{2i-1}^2 + p_{2i}^2) + \frac{\omega^2}{4}\sum_{i=1}^{m}(q_{2i} - q_{2i-1})^2 + \sum_{i=0}^{m}(q_{2i+1} - q_{2i})^4,$$

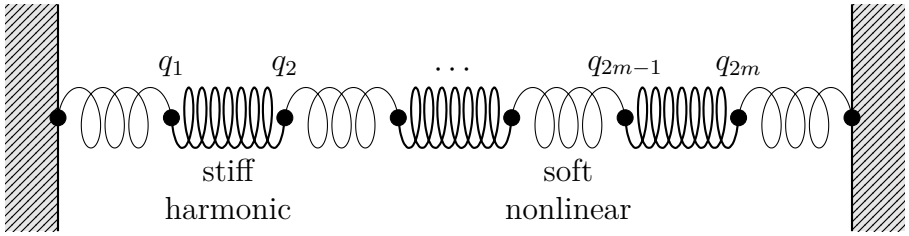

Figure 2: Fermi–Pasta–Ulam test case

with typically $\omega \gg 1$. Introducing the variables

$$x_i = (q_{2i} + q_{2i-1})/\sqrt{2}, \qquad y_i = (p_{2i} + p_{2i-1})/\sqrt{2},$$
$$x_{m+i} = (q_{2i} - q_{2i-1})/\sqrt{2}, \qquad y_{m+i} = (p_{2i} - p_{2i-1})/\sqrt{2},$$

the Hamiltonian can be rewritten as

$$H(\boldsymbol{x}, \boldsymbol{y}) = \frac{1}{2}\sum_{i=1}^{2m} y_i^2 + \frac{\omega^2}{2}\sum_{i=1}^{m} x_{m+i}^2 + \frac{1}{4}\left((x_1 - x_{m+1})^4 + \sum_{i=1}^{m-1}(x_{i+1} - x_{m+i+1} - x_i - x_{m+i})^4 + (x_m + x_{2m})^4\right). \quad (19)$$

As the system is Hamiltonian, the total energy of the system should be conserved by the numerical scheme. The Fermi–Pasta–Ulam system has yet another quasi-invariant. Letting $I_j(x_{m+j}, y_{m+j}) = \frac{1}{2}\left(y_{m+j}^2 + \omega^2 x_{m+j}^2\right)$ be the oscillatory energy of the jth stiff spring, the total oscillatory energy $I = I_1 + I_2 + \cdots + I_m$ is close to a constant value as proved in [11, p.22]:

$$I(\boldsymbol{x}(t), \boldsymbol{y}(t)) = I(\boldsymbol{x}(0), \boldsymbol{y}(0)) + \mathcal{O}(\omega^{-1}).$$

In our numerical experiment, we set $m = 3$ and $\omega = 50$. Figure 3a (left panel) shows the variation of the oscillating energies and of the pesudo-energy $\tilde{H}^n$ over time for a constant time-step $h = 10^{-3}$. The energy exchange between the oscillatory modes is remarkably similar to the reference solution given in [11, Chap. I.4] and represented in Figure 3b (right panel). The reference solution was computed with high accuracy using a Runge–Kutta 4 integrator with a time-step of $h = 10^{-4}$. In particular, the total oscillatory energy I displays fast oscillations around a fixed constant. The conservation of energy is verified up to machine precision, even with a mid-point quadrature. The results being already very satisfactory, the results computed with higher order quadratures are omitted for brevity. A more detailed study of the influence of the order of quadrature on pseudo-energy conservation is presented in the next section.

3.3 Nonlinear wave equation

The setting comes from [3]. The interval $\Omega = [0, 1]$ represents a one-dimensional string. Let $V : \mathbb{R}^d \to \mathbb{R}$ be the potential energy, with dimension $d = 2$. It is assumed that V verifies the following conditions:

- Smoothness: V is of class C^2;
- Convexity: V is strictly convex;

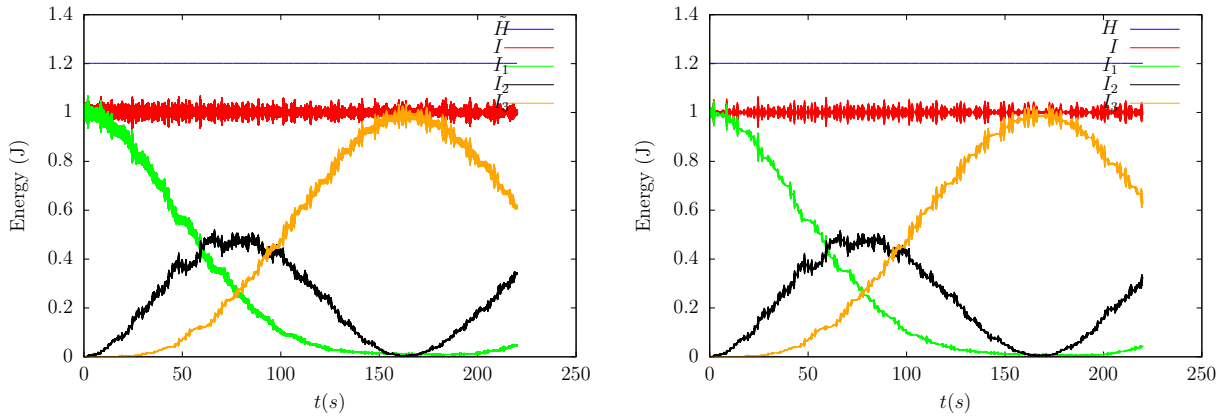

(a) (b)

Figure 3: Fermi–Pasta–Ulam test case: (a) Energy variation, present scheme, $h = 10^{-3}$; (b) reference RK4 solution, $h = 10^{-4}$

- Coercivity: $\exists K > 0$ so that $V(u) \geq K|u|^2$ for all $u \in \mathbb{R}^2$;
- Boundedness: $\exists M > 0$ so that $|\nabla V(u)|^2 \leq M \min(V(u), (1 + |u|^2))$ for all $u \in \mathbb{R}^2$.

The problem of interest is to find $u : \Omega \times \mathbb{R}^+ \to \mathbb{R}^2$ such that

$$\begin{cases} \partial_{tt}^2 u - \partial_x(\nabla V(\partial_x u)) = 0, \\ u(0,t) = 0, \quad u(1,t) = 0, \\ u(x,0) = u^0(x), \quad \partial_t u(x,0) = v^0(x), \end{cases} \tag{20}$$

with given initial conditions $u^0 : \Omega \to \mathbb{R}^2$ and $v^0 : \Omega \to \mathbb{R}^2$. For a pair $(u_1, u_2) \in \mathbb{R}^2$, the functional V takes the following value:

$$V(u_1, u_2) = \frac{u_1^2 + u_2^2}{2} - \alpha \left(\sqrt{(1+u_1)^2 + u_2^2} - (1 + u_1) \right),$$

where the parameter $\alpha \in [0, 1)$ is related to the tension of the string, such that the string behaviour is nonlinear when $\alpha > 0$ and the strength of the nonlinearity increases with α. The following variational formulation in $\mathcal{V} := H_0^1(\Omega; \mathbb{R}^2)$ is considered:

$$\frac{d^2}{dt^2} \left(\int_\Omega \boldsymbol{u} \cdot \boldsymbol{v} \right) + \int_\Omega \nabla V(\partial_x \boldsymbol{u}) \cdot \partial_x \boldsymbol{v} = 0, \quad \forall \boldsymbol{v} \in \mathcal{V}, \ \forall t > 0.$$

We use H^1-conforming $\mathbb{P}_1$ Lagrange finite elements for the space discretization. Let N be the number of nodes discretizing the string and $(\varphi_i)_{1 \leq i \leq 2N}$ be the nodal basis functions associated with the degrees of freedom of the string in the two directions. These basis functions span the finite-dimensional subspace $\mathcal{V}_N \subsetneq \mathcal{V}$. The space semi-discrete function approximating the exact solution is $\boldsymbol{u}_N(t) = \sum_{i=1}^{2N} \boldsymbol{q}_i(t)\varphi_i(x) \in \mathcal{V}_N$ and solves the following space semi-discrete problem:

$$\frac{d^2}{dt^2} \left(\int_\Omega \boldsymbol{u}_N \cdot \boldsymbol{v}_N \right) + \int_\Omega \nabla V(\partial_x \boldsymbol{u}_N) \cdot \partial_x \boldsymbol{v}_N = 0, \quad \forall \boldsymbol{v}_N \in \mathcal{V}_N, \ \forall t > 0.$$

Introducing the vector $\boldsymbol{q} = (q_1, \ldots, q_{2N}) \in \mathbb{R}^{2N}$, the following Hamiltonian system has to be integrated in time:

$$H(\boldsymbol{q}, \boldsymbol{p}) = \frac{1}{2} \boldsymbol{p}^{\mathrm{T}} \boldsymbol{M}^{-1} \boldsymbol{p} + V(\boldsymbol{q}), \qquad V(\boldsymbol{q}) = \int_\Omega V \left(\sum_{i=1}^{2N} \boldsymbol{q}_i \partial_x \varphi_i \right),$$

where $\boldsymbol{M}$ is the classical $\mathbb{P}_1$ Lagrange finite element mass matrix. Assuming that all the components of $\boldsymbol{q}$ associated with the first direction are enumerated first and then those associated with the second direction, the matrix $\boldsymbol{M}$ is a 2×2 block-diagonal matrix and each diagonal block is a tridiagonal matrix of size $N \times N$ equal to $\Delta x\, \text{tridiag}(1/6, 2/3, 1/6)$.

In our numerical experiments, we consider the values $\alpha = 0$ (which corresponds to the linear case), $\alpha = 0.8$ (which corresponds to a mildly nonlinear behavior), and $\alpha = 0.99$ (which corresponds to a strongly nonlinear behavior). The space discretisation is such that $\Delta x = 0.01$ and thus $N = 99$ basis functions are used in each direction. The time-step is $\Delta t = 0.0033$. Using the same space discretisation, the greatest stable constant time-step has been found to be $\Delta t_{\text{max}} = 0.0055$. Three numerical simulations are performed in every case by letting the amplitude of the initial condition u^0 at time t^0 be 0.01, 0.1, or 0.3. The initial velocity at time t^0 is always taken to be zero. The results are reported in Figure 4 where in all cases, a mid-point quadrature is used. Six snapshots of the 2d deformation $u_0(x) + u(x,t)$ of the string over one second are represented horizontally in various colors. The role played by the nonlinearity can be observed in the fact that the amplitude of u^0 influences the vibration of the string. The tension which causes nonlinearity also changes the wave celerity. We observe an excellent agreement between the present results and the results reported in [3].

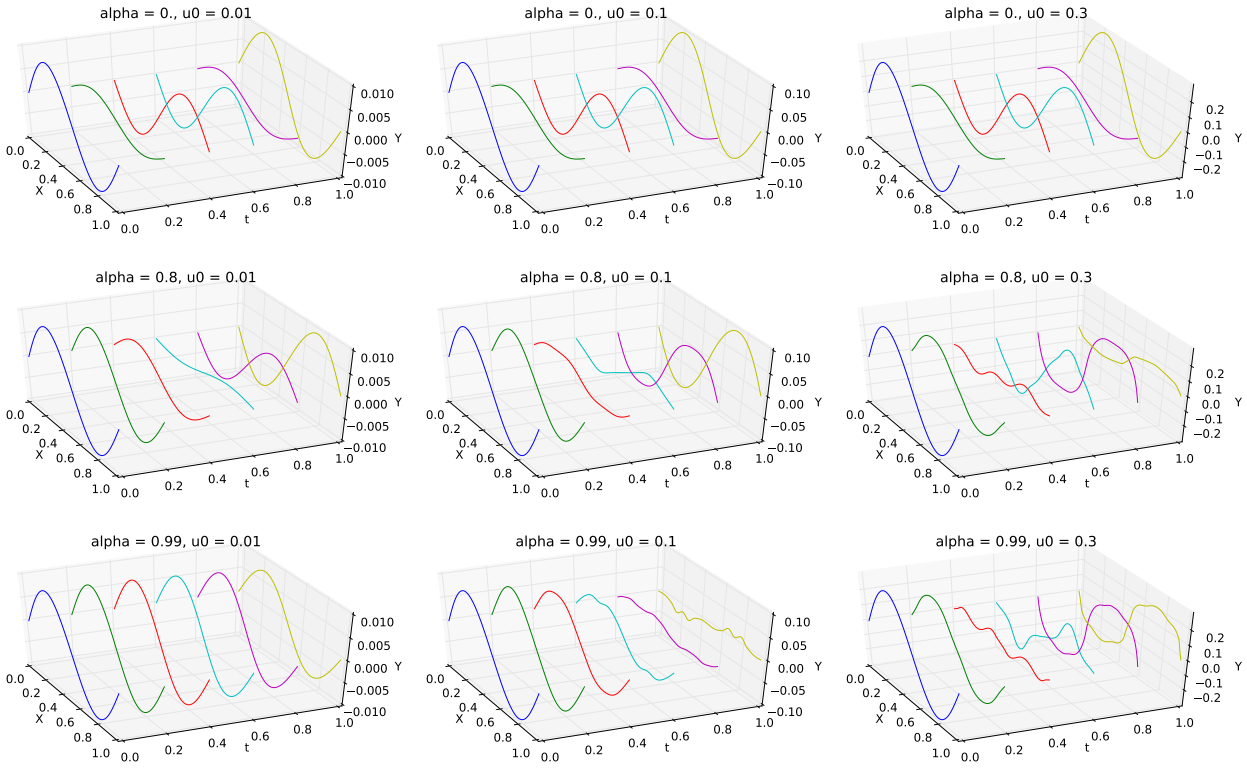

Figure 4: Nonlinear wave equation: Deformations of the string over time with nonlinearity parameter $\alpha = 0$ (top), $\alpha = 0.8$ (middle), and $\alpha = 0.99$ (bottom); the amplitude of u^0 is $u_0 = 0.01$ (left), $u_0 = 0.1$ (middle), and $u_0 = 0.3$ (right)

The time-variation of the discrete pseudo-energy $\tilde{H}^n$ defined by (13) and of the discrete energy H^n defined by (17) are shown in Figure 5a in the most challenging case where $\alpha = 0.99$ and $u^0 = 0.3$. We first observe that the variations the discrete energy H^n are very moderate. In Figure 5b, we illustrate the adaptive time-stepping strategy discussed in Remark 8, where we take $\epsilon_{\text{fly}} = 0.03\%$ to control the departure of $\tilde{H}^n$ from H^n at each

iteration. In this situation, the adaptive time steps take values in the range $[0.0024, 0.005]$. Concerning the pseudo-energy $\tilde{H}^n$, we observe conservation up to machine precision when employing a five-point Gauss–Legendre quadrature of order 9.

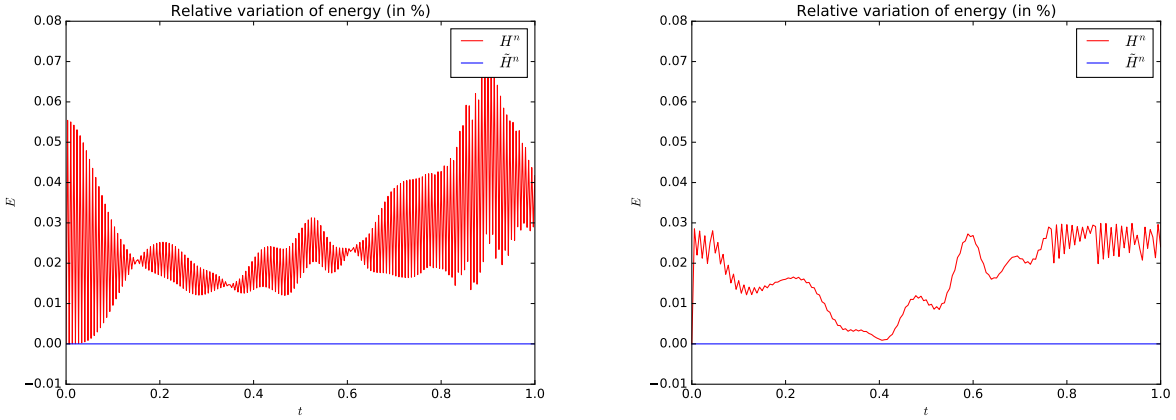

(a) (b)

Figure 5: Nonlinear wave equation: time-variation of the discrete energies H^n and $\tilde{H}^n$ over a unit time interval for $\alpha = 0.99$ and an amplitude of 0.3 for u^0: (a) Fixed time-step $\Delta t = 0.0033$; (b) Adaptive time-step as in Remark 8

α	0			0.8			0.99		
u^0	0.01	0.1	0.3	0.01	0.1	0.3	0.01	0.1	0.3
MP	me	me	me	5.5e-08	5.6e-05	2.4e-05	1.5e-08	1.2e-05	1.1e-04
GL5	me	me	me	1.7e-13	1.2e-14	4.4e-14	3.3e-12	6.4e-13	1.8e-13
GL9	me	me	me	1.6e-13	1.2e-14	me	3.1e-12	me	me

Table 1: Nonlinear wave equation: Maximal errors in the conservation of the pseudo-energy $\tilde{H}^n$ for the mid-point (MP), three-point Gauss–Legendre of order 5 (GL5) and five-point Gauss–Legendre of order 9 (GL9) quadratures; 'me' means machine error

To illustrate the impact of quadratures on pseudo-energy conservation, we perform two numerical experiments. First, Table 1 reports the maximal variation of the pseudo-energy $\tilde{H}^n$ depending on the quadrature used with a constant time-step $\Delta t = 0.0033$. The mid-point quadrature is precise enough when used on the linear equation ($\alpha = 0$). The three-point Gauss–Legendre quadrature of order 5 is found to give very satisfactory results for the two nonlinear cases ($\alpha = 0.8$ and $\alpha = 0.99$). As announced in Remark 2, the maximal error on pseudo-energy conservation is observed to decrease when increasing the quadrature order. The total number of force evaluations is 300, 900, and 1500 when using the mid-point quadrature and the three- and five-point Gauss–Legendre quadratures of order 5 and 9, respectively. In the second experiment, we illustrate the second-order accuracy of pseudo-energy conservation when using the mid-point quadrature. We consider again the most challenging case where $\alpha = 0.99$ and $u^0 = 0.3$. Figure 6 shows the maximal variation of the pseudo-energy $\tilde{H}^n$, defined by (13), with respect to the value of the (fixed) time-step used in the simulation, confirming the second-order accuracy.

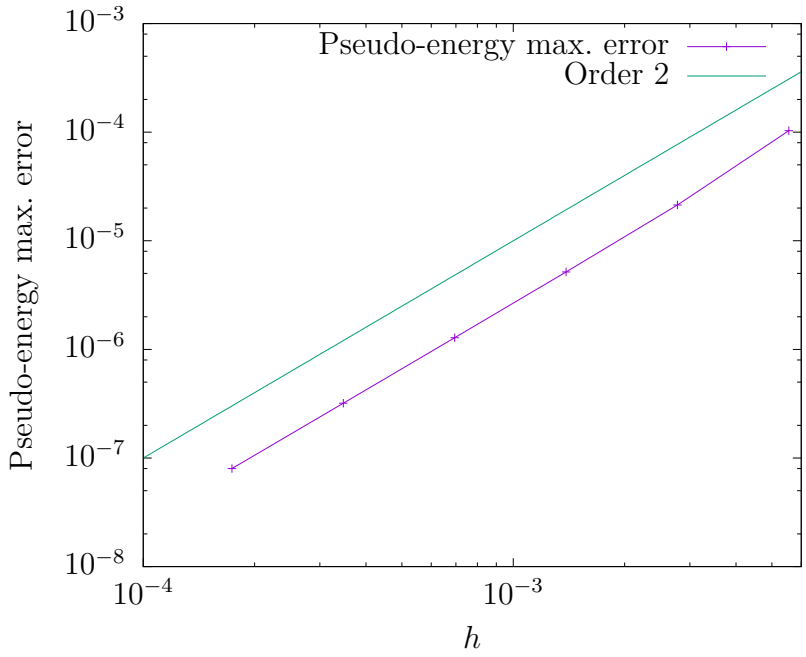

Figure 6: Nonlinear wave equation: Maximal error on pseudo-energy conservation as a function of the time-step in the case $\alpha = 0.99$, $u^0 = 0.3$, and a mid-point quadrature

To conclude this section, we present some comments on the relative costs of the present scheme with respect to an implicit scheme, e.g., the one devised in [3]. In the most challenging case where $\alpha = 0.99$ and $u^0 = 0.3$, the energy conservation in [3] is machine error. For a comparable error, we can consider the present scheme with the five-point Gauss–Legendre quadrature of order 9. The convergence criterion of the Newton's method in the implicit scheme can be estimated to require at least a couple of iterations per time-step and the same number of Hessian computations and global matrix inversions per time-step, whereas the explicit method with the five-point Gauss–Legendre quadrature of order 9 requires only 5 force evaluations per time-step. Thus, although no general conclusions can be drawn, the present explicit method stands good chances to be quite competitive with respect to an implicit method.

4 Asynchronous scheme

Owing to the CFL condition (16), the time-step can be required to be small in regions with stiff or nonsmooth dynamics. The overall efficiency of the computation would be compromised by the large number of integral calculations in the whole domain, while most of these would be redundant in smooth regions. We therefore propose an asynchronous version of the scheme which preserves the general properties of the synchronous version. In this section, we first present the idea behind slow-fast decomposition of the particles and we devise an asynchronous scheme for which we prove pseudo-energy conservation at the slow time nodes under exact force integration. Second-order accuracy is expected and is illustrated numerically on two test cases including an inhomogeneous wave equation.

4.1 Slow-fast splitting

In order to simplify the presentation of the asynchronous scheme, we limit ourselves here to the integration of a slow-fast dynamics, i.e., we consider a system with essentially two distinct time scales. The forces between the particles are supposed to be split into a "fast" set with an associated time-step h_F and a "slow" set with an associated time-step $h_S > h_F$. For example, the splitting can result from the relative stiffness of the forces in the system. Consequently, the particles are split into three sets: the slow particles are subjected only to slow forces, the fast particles are subjected only to fast forces, and the remaining particles, which are called mixed particles, are subjected to both slow and fast forces. This definition means that the slow particles do not interact with the fast particles directly, so that the potential V can be decomposed as follows:

$$V(\boldsymbol{q}) = V_S(\boldsymbol{q}_S) + V_M(\boldsymbol{q}_M, \boldsymbol{q}_S) + V_F(\boldsymbol{q}_F, \boldsymbol{q}_M),$$

where $\boldsymbol{q}_F$, $\boldsymbol{q}_S$, and $\boldsymbol{q}_M$ denote respectively the positions of the fast, slow, and mixed particles, the potential V_S describes the interactions between slow particles, V_M the interactions between slow and mixed particles, and V_F the interactions between mixed and fast particles (or between themselves). For instance, the purple particle in Figure 7 and the Particle 3 in Figure 8 are mixed particles. The mixed particle in Figure 7 is subjected to a "fast" force by the stiff spring on its right and a "slow" force by the soft spring on its left. The fast particle (in red) is only subjected to a "fast" force by the stiff spring. The slow particles (in blue) are only subjected to "slow" forces by the two soft springs. Finding a slow-fast decomposition is not possible for every Hamiltonian system. For example, in the case where all the particles interact with each other, no slow-fast splitting is available. The most favorable configuration is the one where the slow and the fast particles interact essentially among themselves and have very few interactions with mixed particles. This configuration is encountered in inhomogeneous problems where an interface separates two zones where the properties are different; the slow and the fast particles are then located in the two zones, whereas the mixed particles are located at the interface.

In what follows, we abuse the notation by denoting F, M and S the sets collecting the indices in $\{1, \dots, N\}$ of the fast, mixed and slow particles, respectively. For simplicity, we assume that the mass matrix $\boldsymbol{M}$ is diagonal and denote $\boldsymbol{M}_F$, $\boldsymbol{M}_M$ and $\boldsymbol{M}_S$ the restriction of $\boldsymbol{M}$ to the F, M and S particles respectively. Still for simplicity, we assume that both time-steps h_S and h_F are kept constant.

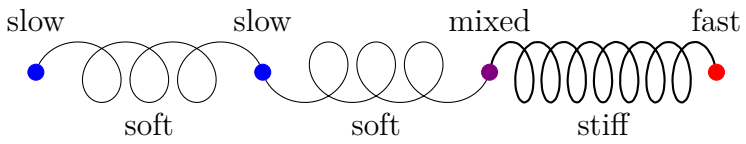

Figure 7: Example of system of particles with a slow-fast splitting

4.2 Presentation of the asynchronous scheme

Without much loss of generality, we can suppose that the slow and fast time-steps are commensurate so that $h_S = Kh_F$ with $K \in \mathbb{N}^*$. We then define the coarse time nodes $t^n = nh_S$ and the fine time nodes $t^{n,m} = t^n + mh_F$ for all $m \in \{0, \dots, K\}$. The asynchronous scheme consists in integrating K times the dynamics of the F and M particles with the

"fast" forces computed at each time-step of length h_F and in updating the S particles with the "slow" forces computed once at the end of each time-step of length h_S. The general procedure is depicted in Figure 8 for four particles in the same configuration as in Figure 7. The efficiency of the asynchronous scheme hinges on the fact that each particle has a free-flight movement during each time-step, with the neighbouring particle forces acting only at the end of the time-step.

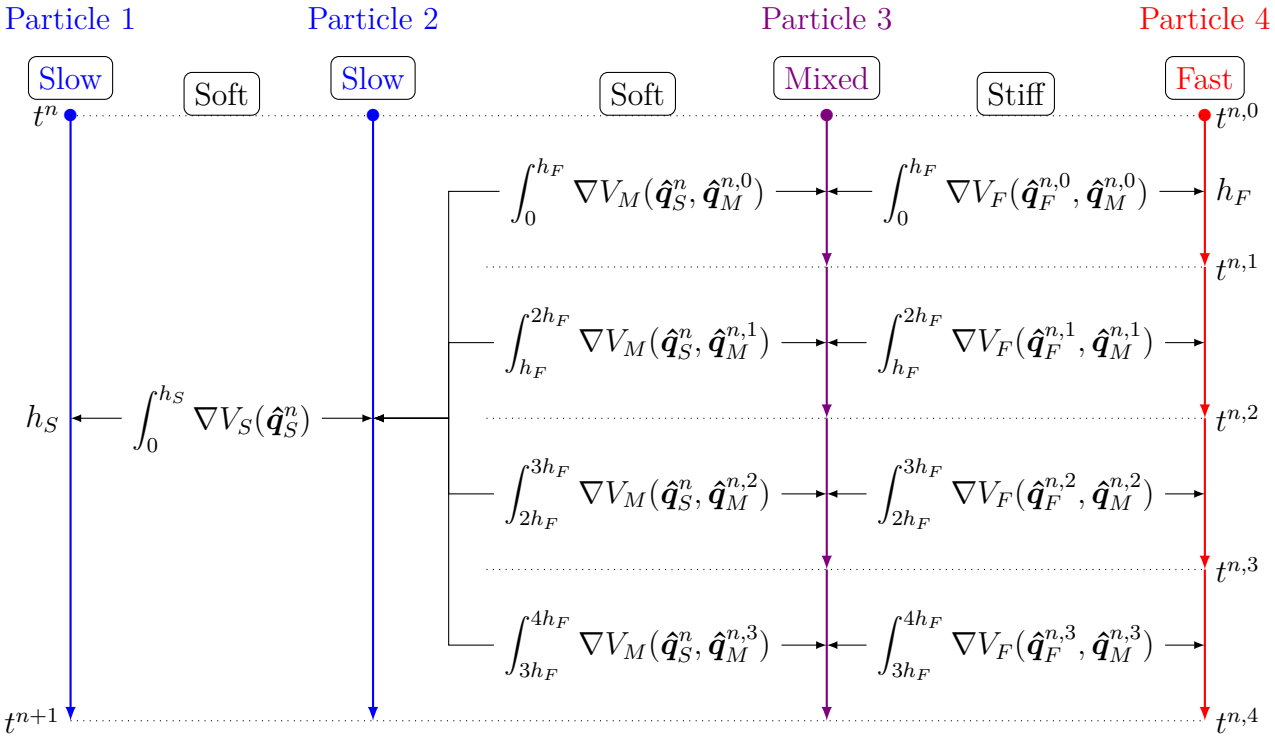

Figure 8: Asynchronous integration of four particles with a slow-fast synamics, $h_S = 4h_F$

Let us now describe in more detail the asynchronous scheme over the coarse time interval $I_n = [t^n, t^{n+1}]$. At the beginning, we have at our disposal the triple $(p_i^{n-1/2}, q_i^n, p_i^{n+1/2})$ for the slow particles ($i \in S$) and the triple $(p_i^{n,-1/2} = p_i^{n-1,K-1/2}, q_i^{n,0}, p_i^{n,1/2})$ for the fast and the mixed particles ($i \in F \cup M$). The asynchronous scheme then proceeds as follows (we use here the two-step formulation which reduces to (6) in the synchronous case):

- For the fast particles ($i \in F$), one computes for all $m \in \{0, \dots, K-1\}$,

$$q_i^{n,m+1} = q_i^{n,m} + h_F \frac{1}{m_i} p_i^{n,m+1/2}, \tag{21a}$$

$$p_i^{n,m+3/2} = p_i^{n,m-1/2} - 2 \int_{t^{n,m}}^{t^{n,m+1}} \frac{\partial V_F}{\partial q_i}(\hat{\boldsymbol{q}}_F^{n,m}(t), \hat{\boldsymbol{q}}_M^{n,m}(t)) dt, \tag{21b}$$

  with the free-flight trajectories for the fast and the mixed particles defined as

$$\hat{q}_j^{n,m}(t) = q_j^{n,m} + \frac{1}{m_j} p_j^{n,m+1/2}(t - t^{n,m}), \quad \forall t \in [t^{n,m}, t^{n,m+1}], \ \forall j \in F \cup M. \tag{22}$$

- For the mixed particles ($i \in M$), one computes for all $m \in \{0, \dots, K-1\}$, the position $q_i^{n,m+1}$ as in (21a), whereas equation (21b) is replaced by

$$p_i^{n,m+3/2} = p_i^{n,m-1/2} - 2 \int_{t^{n,m}}^{t^{n,m+1}} \left(\frac{\partial V_F}{\partial q_i}(\hat{\boldsymbol{q}}_F^{n,m}(t), \hat{\boldsymbol{q}}_M^{n,m}(t)) + \frac{\partial V_M}{\partial q_i}(\hat{\boldsymbol{q}}_M^{n,m}(t), \hat{\boldsymbol{q}}_S^{n}(t)) \right) dt, \tag{23}$$

where the free-flight trajectories of the slow particles are computed over the coarse time interval as follows:

$$\hat{q}_j^n(t) = q_j^n + \frac{1}{m_j} p_j^{n+1/2}(t - t^n), \quad \forall t \in [t^n, t^{n+1}],\ \forall j \in S. \tag{24}$$

- For the slow particles ($i \in S$), one computes

$$q_i^{n+1} = q_i^n + h_S \frac{1}{m_i} p_i^{n+1/2}, \tag{25a}$$

$$p_i^{n+3/2} = p_i^{n-1/2} - 2\sum_{m=0}^{K-1} \int_{t^{n,m}}^{t^{n,m+1}} \frac{\partial V_M}{\partial q_i}(\hat{\boldsymbol{q}}_M^{n,m}(t), \hat{\boldsymbol{q}}_S^n(t))dt - 2\int_{t^n}^{t^{n+1}} \frac{\partial V_S}{\partial q_i}(\hat{\boldsymbol{q}}_S^n(t))dt, \tag{25b}$$

with the free-flight trajectories defined above.

Note that the slow forces between slow and mixed particles need to be evaluated at every fine time-step. In the worst case scenario, every slow force links a slow particle with a mixed particle, which results in the asynchronous scheme reverting to the synchronous scheme. Such a case typically occurs when the particles all interact or when the system alternates fast and slow forces. On the other hand, the efficiency of the asynchronous scheme compared to the synchronous scheme is maximal in the case where the mixed particles constitute a small fraction of the particles and their interaction is limited to a small fraction of the slow particles. A typical case is a nearest-neighbour interaction with slow and fast particles located in distinct regions, the mixed particles being confined in a lower dimensional delimiting interface. In the limit of a large number of particles, the computational cost per large time-step h_S reduces to K integrals of the fast forces and one integral of the slow forces.

Proposition 9 (Synchronization of particles)**.** *Assume that the numerical integration is exact. Then the numerical scheme (21)–(25) exactly conserves the following pseudo-energy at the coarse time nodes t^n:*

$$\begin{aligned}\tilde{H}^n = {} & V_S(\boldsymbol{q}_S^n) + V_M(\boldsymbol{q}_M^{n,0}, \boldsymbol{q}_S^n) + V_F(\boldsymbol{q}_F^{n,0}, \boldsymbol{q}_M^{n,0}) \\ & + \sum_{i\in S} \frac{1}{2m_i} \left(p_i^{n-1/2}\right)^{\mathrm{T}} p_i^{n+1/2} + \sum_{i\in F\cup M} \frac{1}{2m_i} \left(p_i^{n,-1/2}\right)^{\mathrm{T}} p_i^{n,1/2}.\end{aligned} \tag{26}$$

Proof. Let us set

$$\begin{aligned}\tilde{H}_S^n = {} & V_S(\boldsymbol{q}_S^n) + \sum_{i\in S} \frac{1}{2m_i} \left(p_i^{n-1/2}\right)^{\mathrm{T}} p_i^{n+1/2}, \\ \tilde{H}_{FM}^{n,m} = {} & V_F(\boldsymbol{q}_F^{n,m}, \boldsymbol{q}_M^{n,m}) + V_M(\boldsymbol{q}_M^{n,m}, \hat{\boldsymbol{q}}_S^n(t^{n,m})) + \sum_{i\in F\cup M} \frac{1}{2m_i} \left(p_i^{n,m-1/2}\right)^{\mathrm{T}} p_i^{n,m+1/2},\end{aligned}$$

for all $m \in \{0, \dots, K\}$, so that $\tilde{H}^n = \tilde{H}_S^n + \tilde{H}_{FM}^{n,0}$. Following the same calculations as in the proof of Theorem 1 for equation (25), we infer that

$$\tilde{H}_S^{n+1} = \tilde{H}_S^n - \sum_{m=0}^{K-1} \int_{t^{n,m}}^{t^{n,m+1}} \frac{\partial V_M}{\partial \boldsymbol{q}_S}(\hat{\boldsymbol{q}}_M^{n,m}(t), \hat{\boldsymbol{q}}_S^n(t)) \cdot \left(\boldsymbol{M}_S^{-1} \boldsymbol{p}_S^{n+1/2}\right) dt.$$

Similarly, for all $m \in \{0, \dots, K-1\}$, using (21) and (23), we have

$$\tilde{H}_{FM}^{n,m+1} = \tilde{H}_{FM}^{n,m} + \int_{t^{n,m}}^{t^{n,m+1}} \frac{\partial V_M}{\partial \boldsymbol{q}_S}(\hat{\boldsymbol{q}}_M^{n,m}(t), \hat{\boldsymbol{q}}_S^n(t)) \cdot \left(\boldsymbol{M}_S^{-1} \boldsymbol{p}_S^{n+1/2}\right) dt,$$

and summing over m, we obtain

$$\tilde{H}_{FM}^{n+1,0} = \tilde{H}_{FM}^{n,K} = \tilde{H}_{F}^{n,0} + \sum_{m=0}^{K-1} \int_{t^{n,m}}^{t^{n,m+1}} \frac{\partial V_M}{\partial \boldsymbol{q}_S}(\hat{\boldsymbol{q}}_M^{n,m}(t), \hat{\boldsymbol{q}}_S^{n}(t)) \cdot \left(\boldsymbol{M}_S^{-1} \boldsymbol{p}_S^{n+1/2} \right) dt,$$

which gives the result. □

Remark 10 (Asynchronous pseudo-energy conservation)**.** *The pseudo-energy $\tilde{H}^n$ of Theorem 1 is not conserved after every integration over a fast time-step h_F in the asynchronous setting. This results from the fact that during a "slow" time-step h_S, the effect of forces has been taken into account for the "fast" particles but not for the "slow" particles.*

4.3 Numerical results

In this section, we present numerical results on the asynchronous scheme. We first consider a variant of the Fermi–Pasta–Ulam system with a slow-fast dynamics and then an inhomogeneous wave propagation problem.

4.3.1 Fermi–Pasta–Ulam system with slow-fast dynamics

We propose a slight variation of the Fermi–Pasta–Ulam test case in order to assess the efficiency of the asynchronous scheme. Contrary to the usual setting where stiff and soft springs alternate, we suppose here that the system is composed of one stiff region and one soft region, delimited by an interface in the middle of the domain. Figure 9 illustrates the setting. There are $(m-1)$ fast particles, 1 mixed particle, and m slow particles.

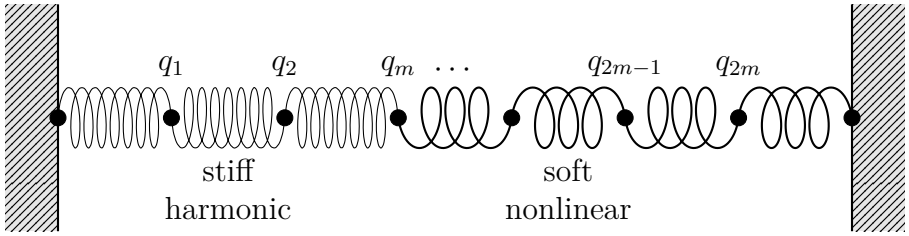

Figure 9: Setting for the Fermi–Pasta–Ulam system with slow-fast dynamics

We consider a problem in dimension $d = 1$. The Hamiltonian is given by

$$H(\boldsymbol{p}, \boldsymbol{q}) = \frac{1}{2} \sum_{i=1}^{2m} p_i^2 + \frac{\omega^2}{4} \sum_{i=1}^{m} (q_i - q_{i-1})^2 + \sum_{i=m}^{2m} (q_{i+1} - q_i)^4.$$

In the present experiment, we take $m = 3$ and $\omega^2 = 10$. The fast forces being generated by stiff linear springs, the fast time-step h_F should respect the CFL condition from Equation (16), which here leads to $h_F \leq 3 \cdot 10^{-3}$. The small time-step h_S being controlled by soft nonlinear springs, the CFL condition (16) is not applicable. A constant stable time-step has been found empirically to be $h_S \leq 10^{-1}$ using the five-point Gauss–Lobatto quadrature of order 7. The dynamics of the particles is presented in Figure 10 for $h_S = 0.01$ and $h_F = 2 \cdot 10^{-4}$, so that 50 iterations of the fine time-step are carried out for each iteration of the coarse time-step. Observe that, as expected, the fast particles ($1 \leq i \leq m$) exhibit oscillations with a typical frequency ω, whereas the slow particles ($m+1 \leq i \leq 2m$) have tame nonlinear oscillations with a frequency smaller than 1. Figure 11 shows

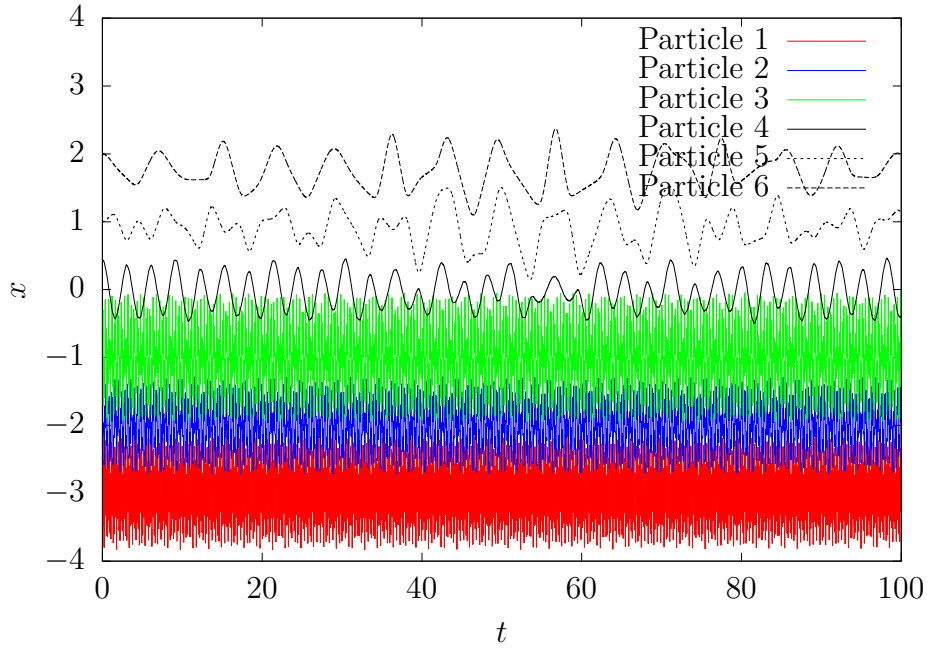

Figure 10: Fermi–Pasta–Ulam system with slow-fast dynamics: Position dynamics for the asynchronous scheme ($h_S = 0.01$, $h_F = 2 \cdot 10^{-4}$)

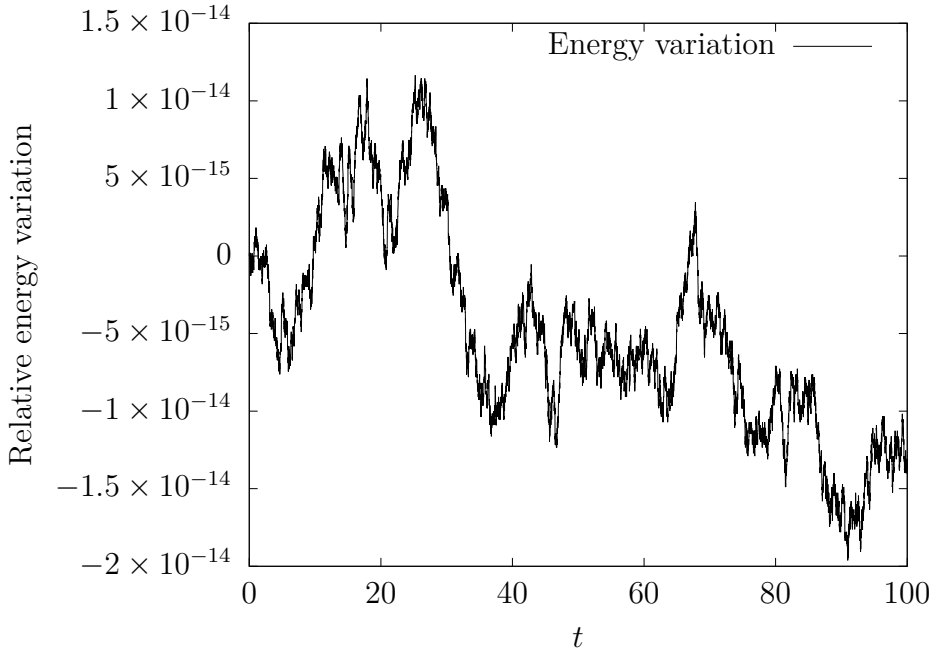

Figure 11: Fermi–Pasta–Ulam system with slow-fast dynamics: Relative variation in the pseudo-energy $\tilde{H}^n$ for the asynchronous scheme ($h_S = 0.01$, $h_F = 2 \cdot 10^{-4}$)

that the pseudo-energy conservation is as perfect for the asynchronous scheme as for the synchronous scheme with the five-point Gauss–Lobatto quadrature of order 7.

The computational cost of the scheme is proportional to the number $\mathcal{N}$ of force evaluations. With an n-point quadrature and a total integration time T, the numbers of force evaluations $\mathcal{N}_s$ and $\mathcal{N}_a$ for the synchronous and asynchronous schemes respectively on the present slow-fast problem are given by:

$$\mathcal{N}_s = (n-1)T\frac{2m+1}{h_F}, \qquad \mathcal{N}_a = (n-1)T\left(\frac{m+1}{h_F} + \frac{m}{h_S}\right).$$

Recalling that $K = \frac{h_S}{h_F} \geq 1$ is the number of fast steps per slow step, the cost reduction η of the asynchronous scheme with respect to the synchronous scheme is given by

$$\eta = \frac{\mathcal{N}_a}{\mathcal{N}_s} = \frac{1 + \frac{m}{(m+1)K}}{1 + \frac{m}{m+1}}.$$

For $h_S = 0.01$, $h_F = 2 \cdot 10^{-4}$ and $T = 100$, $\mathcal{N}_a = 1.015 \cdot 10^8$, to be compared with $\mathcal{N}_s = 1.75 \cdot 10^8$. As m increases,

$$\eta \xrightarrow{m \to +\infty} \frac{1 + \frac{1}{K}}{2}.$$

When the number of fast subiterations K increases, η tends to 0.5, which means that the computational cost reduction of the asynchronous scheme compared to the synchronous scheme approaches 50%. This is the best-case scenario, since the computational cost is concentrated on the fast dynamics where frequent evaluations are required, whereas the slow dynamics is almost costless.

In order to assess the accuracy of the asynchronous scheme, we consider the L^∞-error of the position of the asynchronous solution with respect to the synchronous solution using the small time-step h_F. Figure 12a (left panel) shows the evolution of the error as the coarse time-step h_S is refined, with fixed fine time-step $h_F = 10^{-4}$. We observe a second-order convergence of the error. Figure 12b (right panel) displays the evolution of the error as the fine time-step h_F is further refined, with fixed coarse time-step $h_S = 10^{-2}$. We observe that the error decreases until it reaches a plateau, which is due to the error on the slow particles. These observations confirm that reducing the fine time-step beyond $h_F = h_S/50$ does not significantly improve the error since the error is dominated by the error on the slow particles. Conversely, the error reduction due to the coarse time-step reduction is not compromised by the asynchronous scheme.

Finally, a convergence test is carried out with a constant ratio $\frac{h_S}{h_F} = 25$ and using the five-point Gauss–Lobatto quadrature of order 7. The error is measured as previously by the L^∞-error on the positions between the synchronous and asynchronous schemes. The results are presented in Figure 13. The synchronous method is used with a constant time-step h_F. We observe second-order convergence as both time-steps are refined simultaneously.

4.3.2 Inhomogeneous wave propagation

As a physically relevant example of the slow-fast test case, we consider the propagation of a wave in a linear elastic material in dimension $d = 1$, with an inhomogeneous speed of sound. Denote the domain Ω, $u^0 : \Omega \to \mathbb{R}$ and $v^0 : \Omega \to \mathbb{R}$ initial conditions for

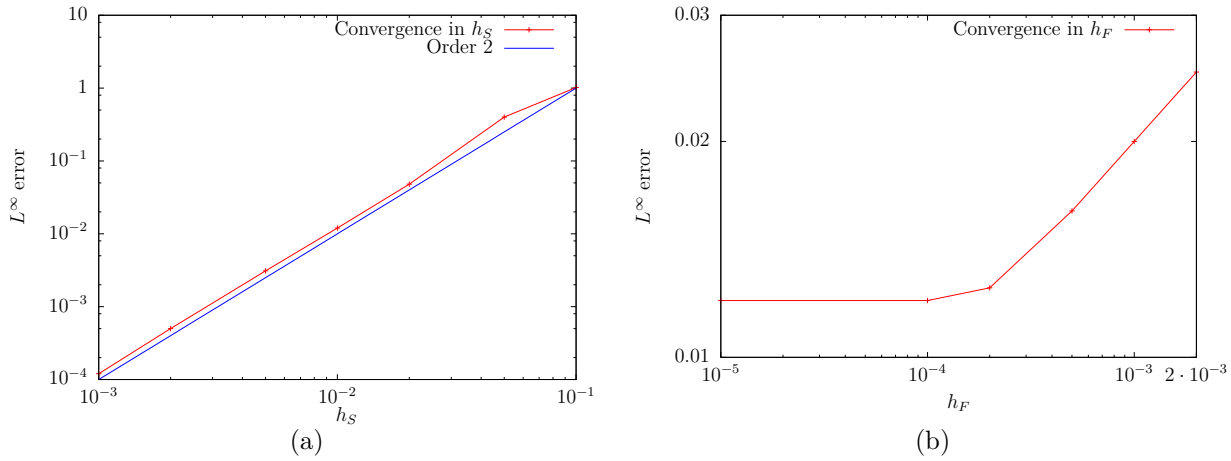

Figure 12: Fermi–Pasta–Ulam system with slow-fast dynamics: Convergence of the asynchronous scheme (a) with respect to the coarse time-step h_S, with fixed fine time-step $h_F = 10^{-4}$, and (b) with respect to the fine time-step h_F, with fixed coarse time-step $h_S = 10^{-2}$

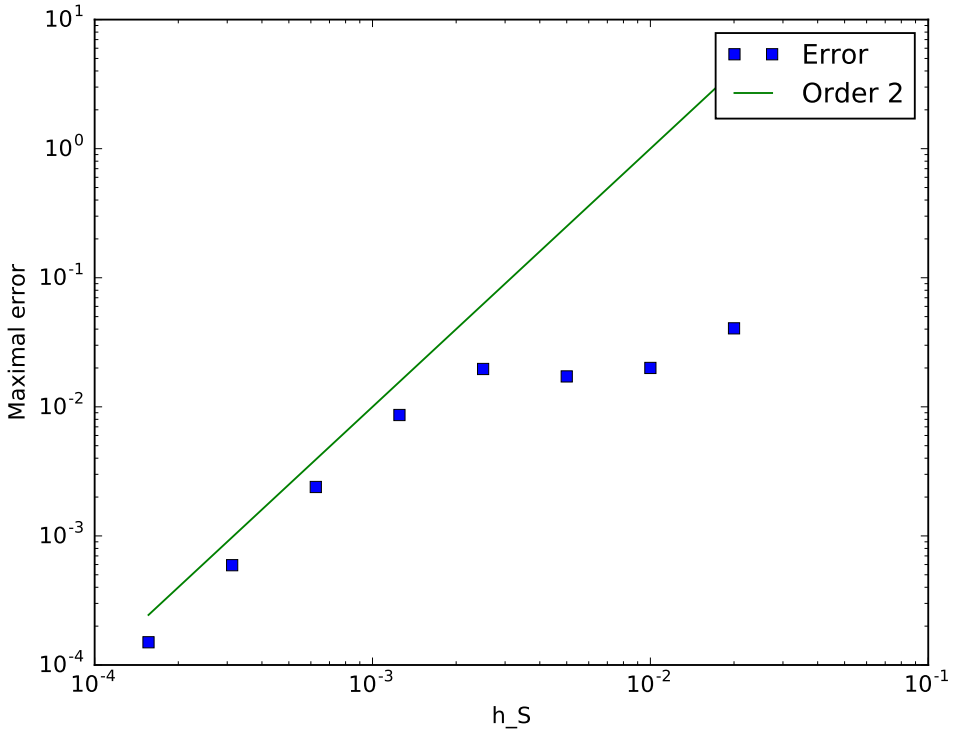

Figure 13: Fermi–Pasta–Ulam system with slow-fast dynamics: L^∞-error on the positions between the synchronous scheme (with time-step h_F) and the asynchronous scheme (with time-steps h_S and h_F having fixed ratio $\frac{h_S}{h_F} = 25$).

displacement and velocity respectively, and $u : \Omega \times \mathbb{R}^+ \to \mathbb{R}$ the displacement, u follows the equations:

$$\begin{cases} \partial_{tt} u = \partial_x \Big(c(x)^2 \partial_x u \Big) & \text{in } \Omega, \\ u_{|\partial\Omega} = 0, \\ u(x,0) = u^0(x), \quad \partial_t u(x,0) = v^0(x). \end{cases} \tag{27}$$

We take $\Omega = (0,1)$ and we set

$$c(x) = \begin{cases} 10 & \text{if } x \leq 0.5, \\ 1 & \text{if } x > 0.5. \end{cases}$$

Setting $N \in \mathbb{N}^*$, $\Delta x = \frac{1}{N}$ and $x_i = i\Delta x$ for all $i \in \{0, \dots, N\}$, the partial differential equation (27) can be semi-discretized in space with the following centered finite difference scheme (which is equivalent to a discretization using H^1-conforming $\mathbb{P}_1$ Lagrange finite elements after lumping the mass matrix):

$$\begin{cases} \dfrac{d^2 u_i}{dt^2} = \dfrac{1}{\Delta x^2} \Big(c(x_{i-1/2})^2 (u_{i-1} - u_i) - c(x_{i+1/2})^2 (u_i - u_{i+1}) \Big) & \text{for } i \in \{1, \dots, N-1\}, \\ u_0 = u_N = 0, \quad \dfrac{du_0}{dt} = \dfrac{du_N}{dt} = 0, \\ u_i(0) = u^0(x_i), \quad \dfrac{du_i}{dt}(0) = v^0(x_i). \end{cases} \tag{28}$$

Setting $\boldsymbol{q} = (u_i)_{0 \leq i \leq N}$, $\boldsymbol{p} = \left(\frac{du_i}{dt}\right)_{0 \leq i \leq N}$ and $\omega_{i-1/2} = \frac{c(x_{i-1/2})}{\Delta x}$, the ordinary differential equation in (28) is derived from the following Hamiltonian:

$$H(\boldsymbol{p}, \boldsymbol{q}) = \frac{1}{2} \sum_{i=1}^{N-1} p_i^2 + \frac{1}{2} \sum_{i=1}^{N} \omega_{i-1/2}^2 (q_i - q_{i-1})^2.$$

The CFL condition (16) becomes

$$h \leq 2 \frac{\Delta x}{\omega_{i-1/2}}, \qquad \forall i \in \{1, \dots, N\}.$$

For the indices i such that $x_i \leq 0.5$, one must then take $h \leq 0.2\Delta x$, while for $x_i > 0.5$, it suffices that $h \leq 2\Delta x$. In what follows, we therefore set the slow (resp. fast) particules as the elements i such that $x_i > 0.5$ (resp. $x_i < 0.5$) and define $h_S = \Delta x$ and $h_F = 0.1\Delta x$. The mixed particle is the particle at the interface between the fast and slow particles.

The numerical solution and the exact solution for the displacement and the velocity computed with $\Delta x = 5 \times 10^{-4}$ are presented in Figures 14 and 15 respectively. The system is initialized with the functions

$$u^0(x) = 10^{-2} e^{-(20(x-0.2))^2} \mathbb{1}_{(0,0.5)}(x), \quad v^0(x) = 8(x-0.2) e^{-(20(x-0.2))^2} \mathbb{1}_{(0,0.5)}(x).$$

The initial condition propagates to the right with the speed of sound $c_1 = 10$, until it reaches $x = 0.5$. At the boundary between the slow and fast domain, it is partly transmitted to the right with speed of sound $c_2 = 1$ and partly reflected with speed $-c_1$. The reflected wave reflects again on the left boundary $x = 0$ of the domain. Successive

reflections and transmissions occur, which result in the final state in Figures 14f and 15f. The exact solution can be expressed as follows for all $t > 0$:

$$\forall x \in (0, 0.5), \quad u(x,t) = \sum_{k\geq 0} \left(\frac{c_2 - c_1}{c_1 + c_2}\right)^k (u_0(x + k - c_1 t) - u_0(k - x - c_1 t)),$$

$$\forall x \in (0.5, 1), \quad u(x,t) = \frac{2c_1}{c_1 + c_2} \sum_{k\geq 0} \left(\frac{c_2 - c_1}{c_1 + c_2}\right)^k u_0 \left(\frac{c_1}{c_2}(x - 0.5) + k + 0.5 - c_1 t\right).$$

The numerical solution matches very well the exact solution. We can observe slight overshoots near the extrema and at the tail of the peaks, especially in the slow domain. This can be explained by the fact that the space-discretization (28) is slightly dispersive so that steep variations tend to generate oscillations (similar to the Gibbs phenomenon). Figure 16 presents the behavior of the error for the asynchronous and synchronous schemes with respect to the number of force evaluations. We consider the maximal error at the end of the simulation, i.e., at $t = 0.5$. The results are obtained by letting $h_S, h_F \to 0$ while keeping the ratio h_S/h_F fixed. The convergence is of order 1 with respect to the number of force evaluations. Since the number of force evaluations scales like $(\Delta x \cdot \Delta t)^{-1}$, this is compatible with a second-order convergence in space and in time after taking into account the CFL condition. In conclusion, the asynchronous scheme displays similar errors to the synchronous scheme, with roughly half of the number of force evaluations involved as noted in Section 4.3.1. This confirms the efficiency of the asynchronous scheme.

5 Conclusion

In this paper, a new explicit pseudo-energy conserving time-integration scheme has been proposed. It is capable of handling general nonlinear Hamiltonian systems and has been tested on classical numerical benchmarks and on a nonlinear wave propagation problem. The present scheme enables the use of local time-stepping strategies to circumvent stiff CFL conditions on the time-step and to enhance computational efficiency in the context of slow-fast dynamics.

Various perspectives of the present work can be considered. We believe that the time-integration of dissipative systems should be a straightforward extension of the present scheme. Variational integrators have been proposed for dissipative systems and have proven to be able to accurately track the physical dissipation of energy [16]. Other possible developments lie in the adaptation of the scheme to constrained Hamiltonian systems [19], such as mechanical contact problems [17, 25] and rigid body rotations [18, 23, 20]. Another perspective is the high-order extension of the present scheme.

Acknowledgements

The authors would like to thank F. Legoll (University Paris-Est, Navier Laboratory) for stimulating discussions on the integration of Hamiltonian dynamics. The authors are also thankful to the anonymous referees for their insightful remarks.

References

[1] M. P. Calvo and J. M. Sanz-Serna. The development of variable-step symplectic integrators, with application to the two-body problem. *SIAM J. Sci. Comput.*, 14:936–952, 1993.

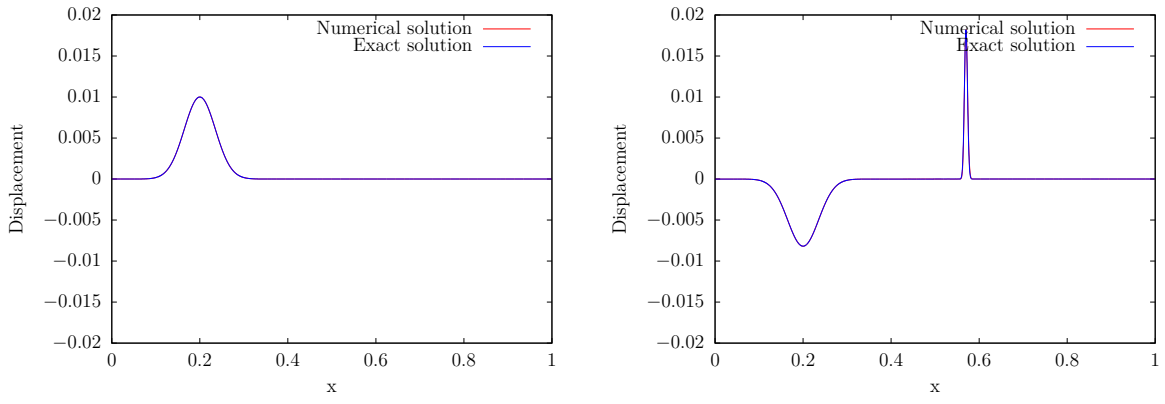

(a) $t = 0$

(d) $t = 0.1$

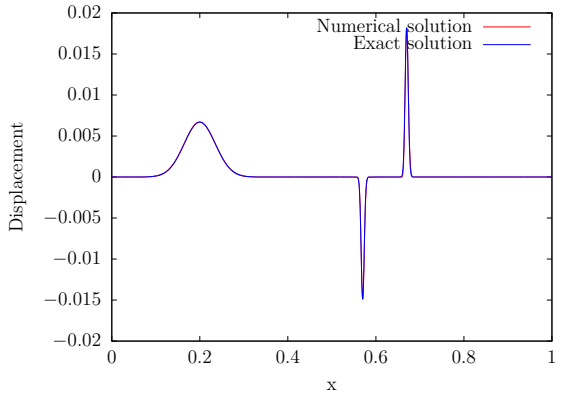

(b) $t = 0.2$

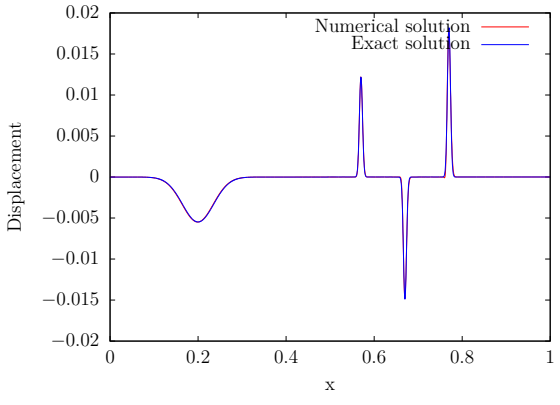

(e) $t = 0.3$

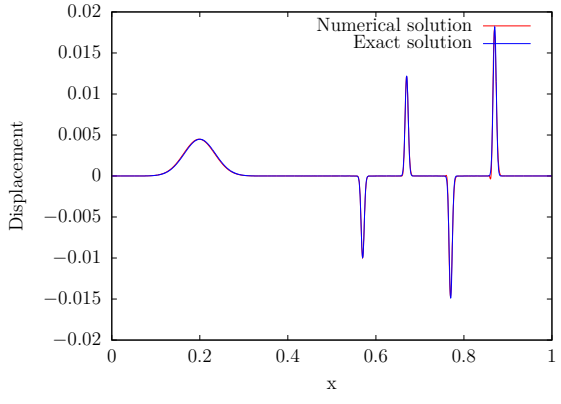

(c) $t = 0.4$

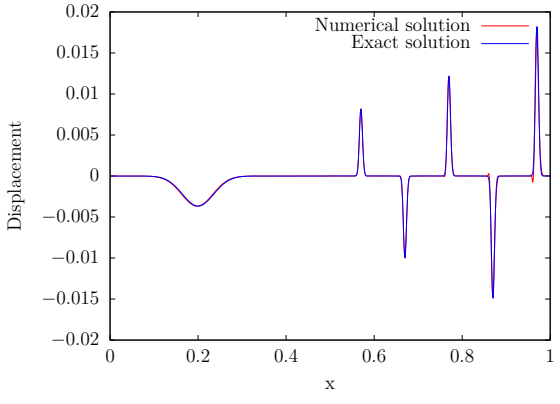

(f) $t = 0.5$

Figure 14: Inhomogeneous wave propagation: Displacement u for $\Delta x = 5 \times 10^{-4}$ at times (a) $t = 0$, (d) $t = 0.1$, (b) $t = 0.2$, (e) $t = 0.3$, (c) $t = 0.4$, (f) $t = 0.5$

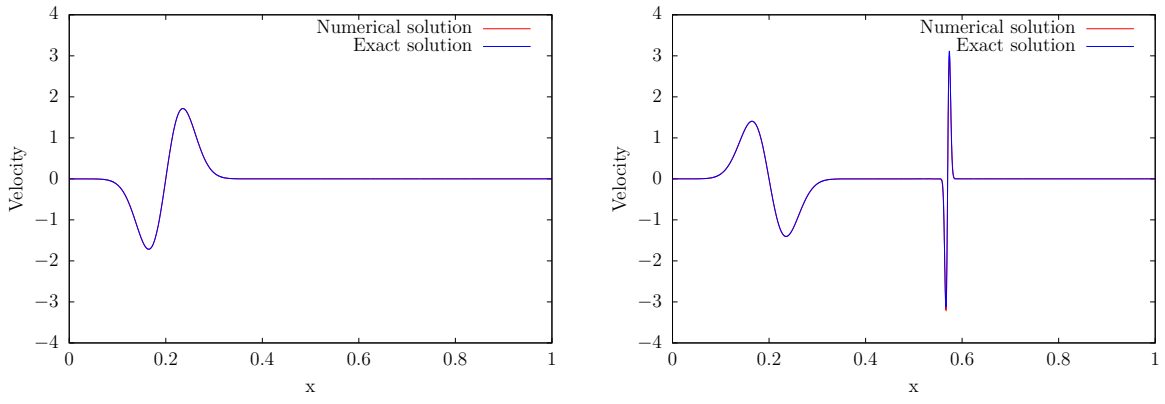

(a) $t = 0$

(d) $t = 0.1$

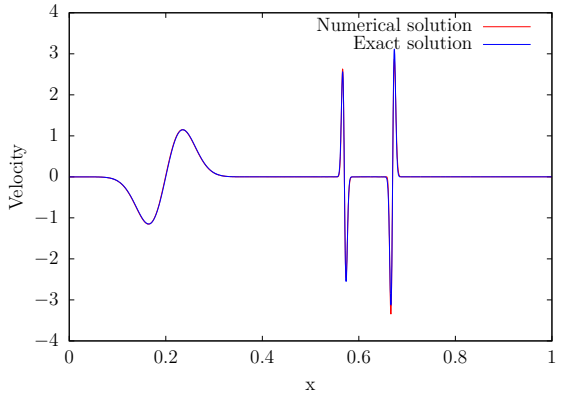

(b) $t = 0.2$

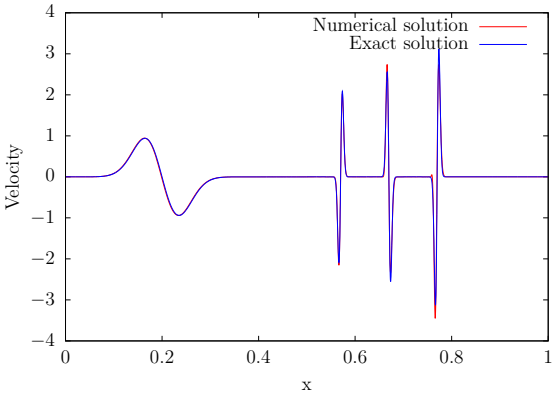

(e) $t = 0.3$

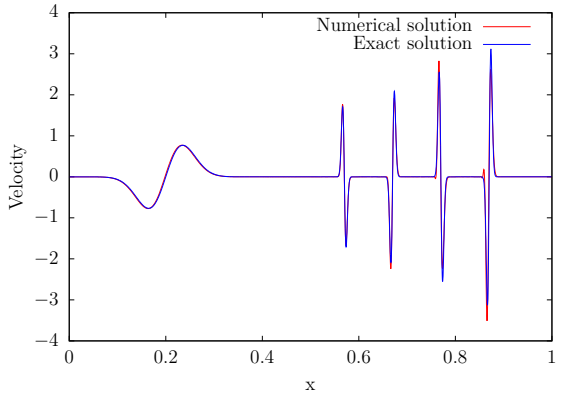

(c) $t = 0.4$

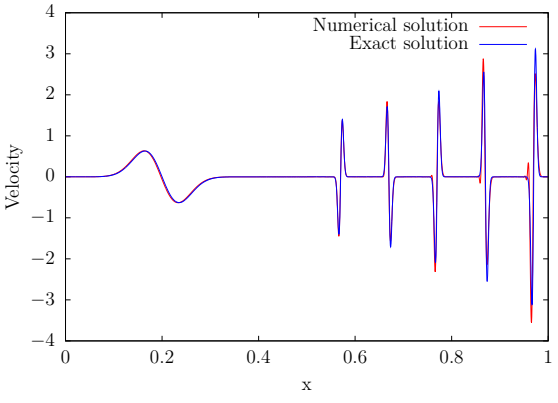

(f) $t = 0.5$

Figure 15: Inhomogeneous wave propagation: Velocity $\frac{du}{dt}$ for $\Delta x = 5 \times 10^{-4}$ at times (a) $t = 0$, (d) $t = 0.1$, (b) $t = 0.2$, (e) $t = 0.3$, (c) $t = 0.4$, (f) $t = 0.5$

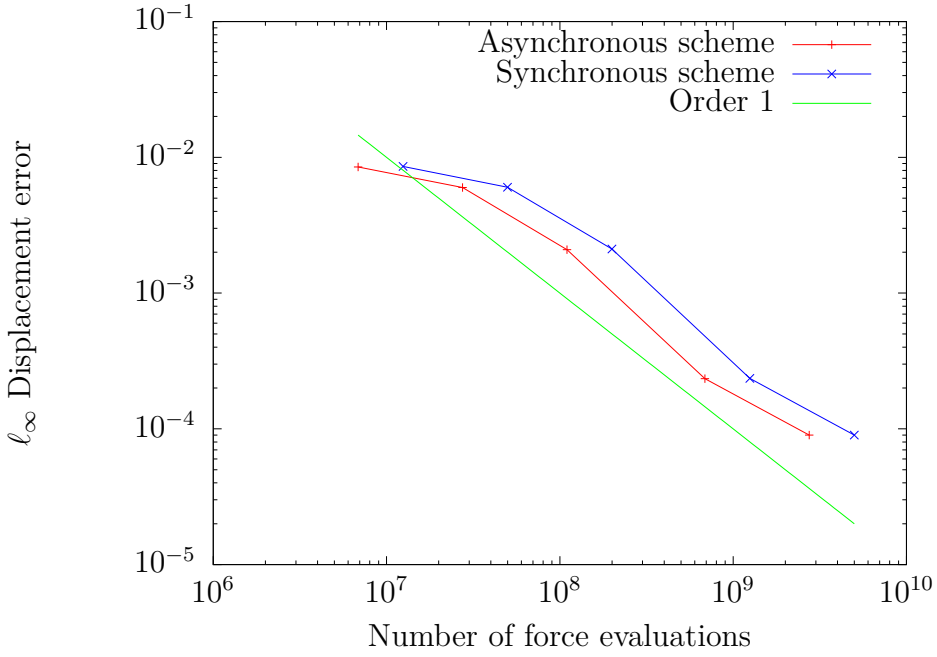

Figure 16: Inhomogeneous wave propagation: Maximal displacement error at $t = 0.5$ against the number of force evaluations for the asynchronous and the synchronous schemes

[2] J. Chabassier and S. Imperiale. Introduction and study of fourth order theta schemes for linear wave equations. *J. Comput. Appl. Math.*, 245:194–212, 2013.

[3] J. Chabassier and P. Joly. Energy preserving schemes for nonlinear Hamiltonian systems of wave equations: Application to the vibrating piano string. *Comput. Methods Appl. Mech. Eng.*, 199(45):2779–2795, 2010.

[4] J. Diaz and M. J. Grote. Energy conserving explicit local time stepping for second-order wave equations. *SIAM J. Sci. Comput.*, 31(3):1985–2014, 2009.

[5] R. C. Fetecau, J. E. Marsden, M. Ortiz, and M. West. Nonsmooth Lagrangian mechanics and variational collision integrators. *SIAM J. Appl. Dyn. Syst.*, 2(3):381–416, 2003.

[6] W. Fong, E. Darve, and A. Lew. Stability of asynchronous variational integrators. *J. Comput. Phys.*, 227(18):8367–8394, 2008.

[7] O. Gonzalez and J. C. Simo. On the stability of symplectic and energy-momentum algorithms for non-linear Hamiltonian systems with symmetry. *Comput. Methods Appl. Mech. Eng.*, 134(3-4):197–222, 1996.

[8] M. Groß, P. Betsch, and P. Steinmann. Conservation properties of a time FE method. part IV: Higher order energy and momentum conserving schemes. *Int. J. Numer. Methods Eng.*, 63(13):1849–1897, 2005.

[9] E. Hairer. Variable time step integration with symplectic methods. *Appl. Numer. Math.*, 25(2-3):219–227, 1997.

[10] E. Hairer. Energy-preserving variant of collocation methods. *J. Numer. Anal. Industr. Appl. Math.*, 5:73–84, 2010.

[11] E. Hairer, C. Lubich, and G. Wanner. *Geometric numerical integration: structure-preserving algorithms for ordinary differential equations*, volume 31. Springer, 2006.

[12] P. Hauret and P. Le Tallec. Energy-controlling time integration methods for nonlinear elastodynamics and low-velocity impact. *Comput. Methods Appl. Mech. Eng.*, 195(37):4890–4916, 2006.

[13] T. J. R. Hughes, W. K. Liu, and P. Caughy. Transient finite element formulations that preserve energy. *J. Appl. Mech*, 45:366–370, 1978.

[14] A. Iserles, H. Z. Munthe-Kaas, S. P. Nørsett, and A. Zanna. Lie-group methods. *Acta Numerica*, 9:215–365, 2000.

[15] C. Kane, J. E. Marsden, and M. Ortiz. Symplectic-energy-momentum preserving variational integrators. *J. Math. Phys.*, 40(7):3353–3371, 1999.

[16] C. Kane, J. E. Marsden, M. Ortiz, and M. West. Variational integrators and the newmark algorithm for conservative and dissipative mechanical systems. *Int. J. Numer. Methods Eng.*, 49(10):1295–1325, 2000.

[17] C. Kane, E. A. Repetto, M. Ortiz, and J. E. Marsden. Finite element analysis of nonsmooth contact. *Comput. Methods Appl. Mech. Eng.*, 180(1):1–26, 1999.

[18] P. Krysl and L. Endres. Explicit Newmark/Verlet algorithm for time integration of the rotational dynamics of rigid bodies. *Int. J. Numer. Methods Eng.*, 62(15):2154–2177, 2005.

[19] S. Leyendecker, J. E. Marsden, and M. Ortiz. Variational integrators for constrained dynamical systems. *ZAMM - Z. Angew. Math. Mech.*, 88(9):677–708, 2008.

[20] C. Mariotti. A new leapfrog scheme for rotational motion in 3d. *Int. J. Numer. Methods Eng.*, 107(4):273–289, 2016.

[21] J. E. Marsden and M. West. Discrete mechanics and variational integrators. *Acta Numerica*, 10:357–514, 2001.

[22] G.R.W. Quispel and D. I. McLaren. A new class of energy-preserving numerical integration methods. *J. Phys. A Math. Theor.*, 41(4):045206, 2008.

[23] J. Salomon, A. A. Weiss, and B. Wohlmuth. Energy-conserving algorithms for a corotational formulation. *SIAM J. Numer. Anal.*, 46(4):1842–1866, 2008.

[24] J. Simo and J. Oliver. A new approach to the analysis and simulation of strain softening in solids. *Fracture Damage Quasibrittle Struct.*, pages 25–39, 1994.

[25] B. Wohlmuth. Variationally consistent discretization schemes and numerical algorithms for contact problems. *Acta Numerica*, 20:569–734, 2011.